

Generation of quantum vortices in photodetachment: The role of the ground-state wave functionF. Cajiao Vélez ^{*}*Institute of Theoretical Physics, Faculty of Physics, University of Warsaw, Pasteura 5, 02-093 Warsaw, Poland* (Received 24 August 2021; revised 8 October 2021; accepted 15 October 2021; published 29 October 2021)

Formation of quantum vortices in laser-induced photodetachment from negative ions is analyzed. The driving laser field consists of a single ultrashort pulse of circular polarization and the unperturbed ground-state wave function of the anion is found in either the s or p state. In particular, numerical illustrations for the photodetachment from H^- , O^- , K^- , and a model A^- anion are presented. Special attention is paid to the symmetry of the ground-state wave function and ionization potential over the final vortex pattern. It is shown that the two-dimensional spectra of photoelectrons in momentum space comprise three well-defined regions: The low-energy (central) region, multiphotonlike zone, and supercontinuum. While the supercontinuum does not contribute to vorticity and the multiphoton zone depends only on the laser field characteristics, vortices in the low-energy region strongly depend on the bound-state wave function and its ionization potential.

DOI: [10.1103/PhysRevA.104.043116](https://doi.org/10.1103/PhysRevA.104.043116)**I. INTRODUCTION**

Electron vortices in quantum mechanics were first described by Dirac in 1931 [1], only a few years after the publication of the Schrödinger equation. In that paper, the author described the fundamental characteristics of electron vortex states by analyzing the general properties of the electron wave function. More than 40 years later, Hirschfelder *et al.* [2–5] revisited Dirac’s findings to explore the formation of matter vortices (originally known as quantum whirlpools) during chemical reactions, molecular collisions, and scattering. This was done from the perspective of the hydrodynamic formulation of quantum mechanics by Madelung [6]. A detailed analysis of vortex structures analyzed under this formulation can be found in, e.g., Refs. [7,8]

During the last decade, a growing interest in the generation and properties of propagating electron vortex states (EVSSs, also known as twisted states) has been observed. EVSSs are characterized by a wave function which circulates around nodal streamlines and carries intrinsic orbital angular momentum (OAM). The OAM is quantized and acquires values of $m\hbar$, where m is an integer number called topological charge or winding number. Moreover, the wave fronts of twisted electrons follow a screwlike path (in position representation) with a vanishing probability at its center [9]. Depending on the type of solution of the Schrödinger equation (in cylindrical coordinates), and the boundary conditions imposed over it, nonrelativistic EVSSs are commonly classified into Bessel states, Laguerre-Gaussian states, bandwidth-limited states, etc. [10–12]. Note, however, that sets of Bessel or Laguerre-Gaussian functions constitute an orthonormal basis; hence, it is in principle possible to decompose any wave function representing an electron beam as a superposition of twisted states [11].

In recent years, another type of electron “vortexlike” structures has received attention. They were originally predicted in photoionization of He atoms driven by two circularly polarized ultrashort laser pulses of opposite handedness [13]. Such structures appear as concentric multiarmed Fermat spirals in the probability distribution of ionization in momentum representation. Their actual shape depends upon the time delay between consecutive laser pulses and their handedness (right-left or left-right circular polarizations) [13]. It was also found that the number of spiral arms varies when two-color driving pulses are used [14]. Those works inspired subsequent papers; such structures were predicted in the double ionization of He [15,16] and single ionization of positive diatomic and triatomic molecular ions [17,18], and have been experimentally observed in photoionization of K atoms [19]. However, it was recently shown that Fermat spirals are not necessarily connected to actual quantum vortices [20]. In particular, the authors showed that, in photodetachment from the H^- ion (s state), a sequence of two counter-rotating driving pulses leads to no vorticity. In contrast, a single and short laser pulse (or series of two corotating pulses) creates rich vortical structures.

In Ref. [21], the authors decomposed the electron wave function showing Fermat spirals into a basis of twisted states. The analysis was carried out for Ne atoms (p orbitals). It was shown that, when two twisted states with opposite topological charge ($\pm m$) interfere along well-defined regions in momentum space, multiarmed spirals are clearly observed. This happens when the target atom is found with a magnetic quantum number $m_\ell = 0$. As they argue, for $m_\ell \neq 0$ the resulting electron wave function contains dissimilar contributions from twisted states with positive and negative topological charges, leading to blurred spirals. Those observations, together with the analysis developed in Ref. [20], strengthen the idea that Fermat spirals should not be confused with (or named as) vortices; they appear when two twisted states with opposite topological charges contribute equally to the final electron wave function. Therefore, the total OAM vanishes at each

^{*}felipe.cajiao-velez@fuw.edu.pl

point in momentum space and no actual electron vortices are formed. It is, however, possible to find both vortices and spiral-like (blurred) structures. This happens when the topological charges in the OAM decomposition do not cancel each other (e.g., when the atom or ion has $m_\ell \neq 0$).

The use of two consecutive and opposite circularly polarized driving pulses hinders the formation of quantum vortices when the unperturbed target ion (atom) is found in the s state. Moreover, laser fields consisting of two identical pulses lead to additional nodal lines in the probability distribution of photoelectrons but no new vortices are expected to appear [20]. Hence, the most favorable condition for the creation of quantum vortices is met when photodetachment is driven by single laser pulses, or more exotic trains of pulses with different handedness [23].

The essence of theoretical physics is the analysis and understanding of complex processes. Usually such physical phenomena are influenced by (and depend upon) a large number of parameters and variables. It is usually desirable to minimize the number of key variables, such that the complexity of the analysis diminishes. Scientists create a “controlled environment” where only certain parameters are allowed to vary. In doing so, the problem under consideration becomes tractable and a suitable model can be constructed. Once the underlying mechanisms governing the phenomenon are found, other variables can be incorporated into the model. In this spirit, we shall present here a theoretical analysis of the formation of quantum vortices in photodetachment. We base our calculations on the strong-field approximation (SFA) [24–26] (further extended by Gribakin and Kuchiev [27] to treat photodetachment) and we shall focus mainly on the influence of the ground-state wave function of the target ion upon the resulting electron vortices. Namely, other key parameters in photodetachment (e.g., polarization, frequency, and duration of the driving field) are kept unchanged while we investigate the vortex formation from anions in the s or p state. Note that in Ref. [22], the authors analyzed the strong-field photoionization from neutral atoms driven by linearly or circularly polarized laser fields. Special emphasis was made upon the influence of the laser pulse characteristics over the final OAM of the freed electron. Particularly, by determining the probability amplitude of ionization under the SFA, the OAM conservation relations were obtained there. Even though their main analysis relates to a “simple” ground-state wave function (i.e., the bound electron is characterized by a magnetic quantum number $m_\ell = 0$), some extrapolations to other states were also made. It is the aim of this paper to extend the investigations initiated there and in Refs. [20,21,23].

This paper is organized as follows. In Sec. II we introduce the main concepts in quantum vorticity by presenting Dirac’s findings [1] in a more modern language. We also introduce the definition of topological charges (Sec. II B) and show how to calculate them in position representation. Its extension to the three-dimensional (3D) momentum space [20,28] is shown in Sec. III D. A general expression for the probability amplitude of photodetachment, in the framework of the SFA, is presented in Sec. III. In particular, we calculate this amplitude in the length gauge (Sec. III A) for wave functions in either the s

or p state (Sec. III B) according to the short-range potential model [27,29]. In Sec. IV we introduce the driving laser pulse used in our calculations and determine its time and frequency properties. Our numerical results are presented in Sec. V. We analyze photodetachment from the H^- and an A^- “toy model” (Sec. V A), and for the O^- (Sec. V B) and K^- (Sec. V C) anions. The total probabilities of detachment are presented in Sec. V D. Finally, in Sec. VI we summarize our main conclusions.

We use atomic units (a.u.) throughout this paper. While we set $\hbar = 1$, in our derivations we show the electron mass, m_e , and charge, $e = -|e|$, explicitly. Our numerical illustrations are presented in terms of the atomic units of momentum, $p_{\text{at}} = \alpha m_e c$; electric field, $\mathcal{E}_{\text{at}} = p_{\text{at}}^3 / (|e| \hbar m_e)$; intensity, $I_{\text{at}} = \varepsilon_0 c \mathcal{E}_{\text{at}}^2$; and energy, $E_{\text{at}} = p_{\text{at}}^2 / m_e$. Here, α represents the fine-structure constant and ε_0 is the permittivity of free space. Also, c represents the speed of light. We take the conversion factors of intensity and energy as $I_{\text{at}} \approx 7.02 \times 10^{16}$ W/cm² and $E_{\text{at}} \approx 27.21$ eV, respectively.

II. VORTICES IN QUANTUM MECHANICS

In Dirac’s 1931 paper [1], the fundamental properties of vortex states in quantum mechanics were described. Unfortunately, this work remained largely unnoticed for many years. For this reason, we deem it important to present some of his most important results while using a more familiar notation (Sec. II A). In doing so, important concepts necessary for the proper understanding of vortex states are also introduced. In Sec. II B we use such concepts to calculate the topological charges.

A. Dirac’s analysis

Consider an electron moving in the presence of a potential $V_0(\mathbf{r}, t)$. Its wave function, $\psi_0(\mathbf{r}, t)$, satisfies the Schrödinger equation

$$-\frac{1}{2m_e} \nabla^2 \psi_0(\mathbf{r}, t) + eV_0(\mathbf{r}, t) \psi_0(\mathbf{r}, t) = i \frac{\partial}{\partial t} \psi_0(\mathbf{r}, t), \quad (1)$$

and can be written in terms of its modulus and phase, i.e., $\psi_0(\mathbf{r}, t) = R(\mathbf{r}, t) e^{iS_0(\mathbf{r}, t)}$, where $R(\mathbf{r}, t) = |\psi_0(\mathbf{r}, t)|$ and $S_0(\mathbf{r}, t) = \arg[\psi_0(\mathbf{r}, t)]$. It is clear that the addition of integer multiples of 2π to $S_0(\mathbf{r}, t)$ would leave $\psi_0(\mathbf{r}, t)$, and any physical observables related to it, unchanged. Furthermore, the continuity condition inherent to the wave function also remains valid. Assume now that there is a linear transformation T which adds an undefined phase $\Lambda(\mathbf{r}, t)$ to all states in the Hilbert space. In particular, $\psi_0(\mathbf{r}, t) \xrightarrow{T} \psi(\mathbf{r}, t)$ with

$$\psi(\mathbf{r}, t) = \psi_0(\mathbf{r}, t) e^{i\Lambda(\mathbf{r}, t)} = R(\mathbf{r}, t) e^{iS(\mathbf{r}, t)}, \quad (2)$$

and $S(\mathbf{r}, t) = S_0(\mathbf{r}, t) + \Lambda(\mathbf{r}, t)$. As the additional phase is independent of any particular state, and common to all of them, the transformation T should be related to the introduction of an external force field acting upon the whole system. If $\psi(\mathbf{r}, t)$ describes the state of an electron moving in the presence of the potential $V_0(\mathbf{r}, t)$, it must satisfy the Schrödinger equation

$$-\frac{1}{2m_e} \nabla^2 \psi(\mathbf{r}, t) + eV_0(\mathbf{r}, t) \psi(\mathbf{r}, t) = i \frac{\partial}{\partial t} \psi(\mathbf{r}, t). \quad (3)$$

From Eqs. (2) and (3) it is easy to show that the following equation is also satisfied:

$$\frac{1}{2m_e}[-i\nabla + \boldsymbol{\alpha}(\mathbf{r}, t)]^2\psi_0(\mathbf{r}, t) + e[V_0(\mathbf{r}, t) + \frac{1}{e}\alpha_0(\mathbf{r}, t)]\psi_0(\mathbf{r}, t) = i\frac{\partial}{\partial t}\psi_0(\mathbf{r}, t), \quad (4)$$

where $\boldsymbol{\alpha}(\mathbf{r}, t) = \nabla\Lambda(\mathbf{r}, t)$ and $\alpha_0(\mathbf{r}, t) = \partial_t\Lambda(\mathbf{r}, t)$.

By comparing Eqs. (1) and (4) it becomes clear that the multiplication of $\psi_0(\mathbf{r}, t)$ by the Dirac phase $e^{i\Lambda(\mathbf{r}, t)}$ introduces a change in the electron momentum given by $\boldsymbol{\alpha}(\mathbf{r}, t)$, together with a change in potential proportional to $\alpha_0(\mathbf{r}, t)$. This is equivalent to the introduction of an electromagnetic field external to our system. Such a field is defined by a vector potential $-e\mathbf{A}(\mathbf{r}, t) = \boldsymbol{\alpha}(\mathbf{r}, t)$ and a scalar potential $eV_1(\mathbf{r}, t) = \alpha_0(\mathbf{r}, t)$. The electric and magnetic fields compatible with them are therefore given by

$$\mathcal{E}(\mathbf{r}, t) = -\frac{1}{e}\nabla\alpha_0(\mathbf{r}, t) + \frac{1}{e}\frac{\partial}{\partial t}\boldsymbol{\alpha}(\mathbf{r}, t), \quad (5)$$

$$\mathcal{B}(\mathbf{r}, t) = -\frac{1}{e}\nabla \times \boldsymbol{\alpha}(\mathbf{r}, t), \quad (6)$$

respectively.

It is now interesting to calculate the changes in phase $\Lambda(\mathbf{r}, t)$ along a closed curve \mathcal{C} . This is done by integrating $\nabla\Lambda(\mathbf{r}, t) = \boldsymbol{\alpha}(\mathbf{r}, t)$ around \mathcal{C} , i.e.,

$$\begin{aligned} \Delta\Lambda_{\mathcal{C}} &= \oint_{\mathcal{C}} \boldsymbol{\alpha}(\mathbf{r}, t) \cdot d\mathbf{r} = \int_{\mathcal{S}} [\nabla \times \boldsymbol{\alpha}(\mathbf{r}, t)] \cdot d\mathbf{s} \\ &= -e \int_{\mathcal{S}} \mathcal{B}(\mathbf{r}, t) \cdot d\mathbf{s}, \end{aligned} \quad (7)$$

where the right-hand-side integral is calculated over the area \mathcal{S} enclosed by the contour \mathcal{C} . In other words, the change in phase $\Delta\Lambda_{\mathcal{C}}$ around a closed loop is proportional to the magnetic flux across \mathcal{S} .

From this observation, Dirac concluded that the changes in phase are determined by the magnetic flux plus an additional $\Lambda_m = 2\pi m$. Consider now a circular loop in the 3D space with vanishing radius ρ . The magnetic flux through the surface $\mathcal{S} = \pi\rho^2$ vanishes and, from the continuity of the wave function, only infinitesimally small changes in its phase are possible. This implies that the only additional phase Λ_m must be $\Lambda_0 = 0$.

Suppose that there is a point where both the real and imaginary parts of the wave function vanish. A collection of such points in the 3D space forms continuous nodal lines (or surfaces) characterized by a vanishing probability density and a singular phase. If the infinitesimally small contour surrounds one of such lines, the change in phase of the wave function around \mathcal{C} does not have to be small, as the continuity conditions for the phase do not apply anymore. In fact, it can take a value close to Λ_m with m not necessarily equal to zero [1]. Dirac already recognized the integer m as an intrinsic property of the particular nodal line [30]. In modern terminology m is known as the topological charge (see, e.g., Refs. [10–12]).

The generalization of those findings to an arbitrary contour is straightforward; the total change in phase of the wave function along a closed path \mathcal{C} and encircling N nodal lines with

topological charges m_i is given by [1]

$$\oint_{\mathcal{C}} \nabla S(\mathbf{r}, t) \cdot d\mathbf{r} = 2\pi \sum_{i=0}^N m_i - e \int_{\mathcal{S}} \mathcal{B}(\mathbf{r}, t) \cdot d\mathbf{s}. \quad (8)$$

Even though this fundamental result was derived from the properties of a wave function in position representation, it can be extended to an arbitrary three-dimensional space (see below).

B. Calculation of the topological charge

The aim of this paper is to analyze the formation of vortices in photodetachment driven by a short laser pulse. After the interaction with the pulse is over, both the electric and magnetic fields vanish. Hence, at times $t \geq T_p$ (with T_p being the duration of the laser pulse), the change in phase of the wave function $\psi(\mathbf{r}, t)$ around the contour \mathcal{C} is only determined by the number of nodal lines encircled by it and their individual topological charges, i.e.,

$$\oint_{\mathcal{C}} \nabla S(\mathbf{r}, t) \cdot d\mathbf{r} = 2\pi \sum_{i=0}^N m_i. \quad (9)$$

With the wave function written in terms of the two real functions $R(\mathbf{r}, t)$ and $S(\mathbf{r}, t)$ [see Eq. (2)] it follows directly that

$$\text{Re}(\psi^*(\mathbf{r}, t)[-i\nabla]\psi(\mathbf{r}, t)) = R^2(\mathbf{r}, t)\nabla S(\mathbf{r}, t). \quad (10)$$

Hence, from Eq. (9) we obtain the following relation:

$$\oint_{\mathcal{C}} \frac{\text{Re}(\psi^*(\mathbf{r}, t)[-i\nabla]\psi(\mathbf{r}, t))}{|\psi(\mathbf{r}, t)|^2} \cdot d\mathbf{r} = 2\pi \sum_{i=0}^N m_i. \quad (11)$$

The symmetry of our problem calls for a treatment in cylindrical coordinates. The topological charges are calculated for a circular loop parallel to the laser field polarization plane (i.e., the xy plane) of radius ρ_r and center at the z axis. With $\boldsymbol{\rho} = (\rho_r \cos \varphi, \rho_r \sin \varphi, \rho_z)$ and taking ρ_r and ρ_z constant, Eq. (11) takes the form [20]

$$m(\rho_r, \rho_z, t) = \frac{1}{2\pi} \int_0^{2\pi} d\varphi \frac{\text{Im}(\psi^*(\boldsymbol{\rho}, t)\partial_{\varphi}\psi(\boldsymbol{\rho}, t))}{|\psi(\boldsymbol{\rho}, t)|^2}. \quad (12)$$

Here, $m(\rho_r, \rho_z, t)$ is the total topological charge enclosed by a circle of radius ρ_r at times $t \geq T_p$.

III. PROBABILITY AMPLITUDE OF DETACHMENT

We consider the photodetachment of a negatively charged ion driven by a single ultrashort laser pulse. In our derivations, we use both the single-active electron approximation and the dipole approximation. It is assumed that at times $t < 0$ the ion is in its unperturbed ground state. The outermost electron is described by the stationary state $|\Phi_0\rangle$ with energy E_0 , such

that

$$\hat{H}_0|\Phi_0\rangle = E_0|\Phi_0\rangle, \quad (13)$$

where

$$\hat{H}_0 = \frac{\hat{\mathbf{p}}^2}{2m_e} + eV_{\text{SR}}(\hat{\mathbf{r}}) \quad (14)$$

is the ionic Hamiltonian, $\hat{\mathbf{p}}$ is the momentum operator, and $V_{\text{SR}}(\mathbf{r})$ is a short-range effective potential experienced by the electron. When the laser pulse acts over the target anion (i.e., at times $t \in [0, T_p]$), the full Hamiltonian governing the electron dynamics is given by

$$\hat{H}(t) = \hat{H}_0 + \hat{H}_I(t). \quad (15)$$

Here $\hat{H}_I(t)$ is the gauge-dependent interaction Hamiltonian (which accounts for the interaction with the light field) and vanishes at $t < 0$ and $t > T_p$. It is assumed that at $t \geq T_p$ the freed electron is found in the exact scattering state $|\Psi_{\mathbf{p}}(t)\rangle$ with asymptotic momentum \mathbf{p} . This state contains information about the interaction of the electron with both the effective potential and the laser field during its whole evolution. Its analytical expression is, in general, unknown.

The probability amplitude of detachment, $\mathcal{A}(\mathbf{p})$, from the ground state $|\Phi_0\rangle$ to the scattering state $|\Psi_{\mathbf{p}}(t)\rangle$ has been previously calculated (see, e.g., Refs. [23,27,31]) and it is given by

$$\mathcal{A}(\mathbf{p}) = -i \int_0^{T_p} dt \langle \Psi_{\mathbf{p}}(t) | \hat{H}_I(t) | \Phi_0(t) \rangle, \quad (16)$$

where $|\Phi_0(t)\rangle = |\Phi_0\rangle \exp(-iE_0t)$. The essence of the SFA consists in approximating the exact scattering state by the Volkov solution of the electron in the laser field [32]. Namely, it is assumed that the freed electron does not interact with the parent ion (or neutral atom) after its promotion to the continuum [33]. Hence, under the SFA framework, the probability amplitude of detachment reads

$$\mathcal{A}(\mathbf{p}) \approx -i \int_0^{T_p} dt \langle \psi_{\mathbf{p}}(t) | \hat{H}_I(t) | \Phi_0(t) \rangle, \quad (17)$$

where $|\psi_{\mathbf{p}}(t)\rangle$ represents the gauge-dependent Volkov state. The introduction of such state, however, breaks the gauge invariance of the theory; different predictions are expected depending on whether the velocity or length gauges are used.

A. Probability amplitude in the length gauge

The probability amplitude in the SFA, as presented in Eq. (17), is very general. The interaction Hamiltonian, $\hat{H}_I(t)$, and the Volkov state $|\psi_{\mathbf{p}}(t)\rangle$ can be determined either in the length or the velocity gauges. Our aim here is to calculate the probability amplitude of photodetachment in the length gauge (as suggested by Gribakin and Kuchiev in Ref. [27]) when the target anion is found in the s or p state. In this gauge, the Volkov solution takes the form [31,32]

$$|\psi_{\mathbf{p}}^L(t)\rangle = |\mathbf{p} - e\mathbf{A}(t)\rangle \times \exp\left[-i \int_0^t dt' \left[\frac{1}{2m_e} (\mathbf{p} - e\mathbf{A}(t'))^2 \right], \quad (18)$$

and the interaction Hamiltonian reads

$$\hat{H}_I(t) = -e\mathcal{E}(t) \cdot \hat{\mathbf{r}}. \quad (19)$$

Note that $\mathcal{E}(t) = -\partial_t \mathbf{A}(t)$ is the oscillating electric field defining the laser pulse and $\mathbf{A}(t)$ is the corresponding vector potential.

From Eqs. (18) and (19), the probability amplitude of detachment [Eq. (17)] can be written as [23,31]

$$\mathcal{A}(\mathbf{p}) = ie \int_0^{T_p} dt \mathcal{E}(t) \cdot \tilde{\Phi}_0(\mathbf{p} - e\mathbf{A}(t)) e^{iG(\mathbf{p},t)}, \quad (20)$$

with

$$G(\mathbf{p},t) = \int_0^t dt' \left[\frac{1}{2m_e} (\mathbf{p} - e\mathbf{A}(t'))^2 - E_0 \right]. \quad (21)$$

For simplicity, we have also introduced the function $\tilde{\Phi}_0(\mathbf{p})$ evaluated at the kinetic momentum $\mathbf{p} - e\mathbf{A}(t)$. It is defined as

$$\tilde{\Phi}_0(\mathbf{p}) = \int d^3r \mathbf{r} \Phi_0(\mathbf{r}) e^{-i\mathbf{p}\cdot\mathbf{r}} = i\nabla_{\mathbf{p}} \tilde{\Phi}_0(\mathbf{p}), \quad (22)$$

where $\nabla_{\mathbf{p}}$ is the gradient calculated in momentum coordinates and $\tilde{\Phi}_0(\mathbf{p})$ is the Fourier transform of the ground-state wave function $\Phi_0(\mathbf{r}) = \langle \mathbf{r} | \Phi_0 \rangle$. According to the convention adopted in this paper, the Fourier transform from position to momentum coordinates is defined as

$$\tilde{\Phi}_0(\mathbf{p}) = \int d^3r e^{-i\mathbf{p}\cdot\mathbf{r}} \Phi_0(\mathbf{r}). \quad (23)$$

In the following, we shall introduce the ground-state wave function for a weakly bound electron in a negative ion, according to the short-range potential model, and calculate $\tilde{\Phi}_0(\mathbf{p})$ [Eq. (22)].

B. s and p states for a negative ion

As it was shown by Gribakin and Kuchiev [27], the photodetachment from negative ions depends, up to a large extent, on the asymptotic form of the ground-state wave function (at least in the length gauge). It was demonstrated that the many-electron interactions happening at short distances from the nucleus do not influence importantly the probability amplitude of detachment and, in fact, can be accounted for by choosing an adequate asymptotic form of the wave function [i.e., by using appropriate parameters A and κ in Eqs. (28) and (29) below]. Furthermore, in Refs. [20,23], the authors corroborated that the SFA gives remarkable qualitative and quantitative results (up to a constant factor) in photodetachment from H^- (s state) when considering only the asymptotic form of the wave function. Their results were compared with the numerical solution of the time-dependent Schrödinger equation (TDSE). For this reason, we shall calculate the probability amplitude of detachment in the SFA only considering the asymptotic form of the bound state.

1. Bound states in a short-range effective potential

We base our further derivations on a short-range potential to model the electron-core interaction. For an electron characterized by the azimuthal and magnetic quantum numbers ℓ and

m_ℓ , respectively, the ground-state wave function reads [29]

$$\Phi_0(\mathbf{r}) \approx A \sqrt{\frac{2\kappa}{\pi}} \frac{K_{\ell+1/2}(\kappa r)}{\sqrt{r}} Y_\ell^{m_\ell}(\theta_r, \varphi_r), \quad (24)$$

where r , θ_r , and φ_r are the magnitude, polar angle, and azimuthal angle defining the position vector \mathbf{r} ; $Y_\ell^m(\theta_r, \varphi_r)$ are the spherical harmonics and $K_{\ell+1/2}(\kappa r)$ are the Macdonald functions (also known as the modified Bessel functions of the second kind). For this particular effective model, two parameters are introduced: The prefactor A , and κ . While the latter relates to the ground-state energy of the anion as

$$E_0 = -E_{\text{at}} \frac{\kappa^2}{2}, \quad (25)$$

the former is a fitting parameter (not a normalization constant) chosen by comparing the expected ion properties with experimental results or other *ab initio* calculations. For a detailed discussion about the coefficient A , we refer the reader to Ref. [34].

For s and p states, we use the analytical expressions for the Macdonald function (see Eqs. 10.47.9 and 10.49.13 in Ref. [35])

$$K_{1/2}(\kappa r) = \sqrt{\frac{\pi}{2\kappa r}} e^{-\kappa r}, \quad (26)$$

$$K_{3/2}(\kappa r) = \sqrt{\frac{\pi}{2\kappa r}} e^{-\kappa r} \left[1 + \frac{1}{\kappa r} \right]. \quad (27)$$

Hence, from Eq. (24), the s -orbital wave function reads

$$\Phi_s(\mathbf{r}) = \frac{A}{r} e^{-\kappa r} Y_0^0(\theta_r, \varphi_r), \quad (28)$$

and for p orbitals ($m_\ell = 0, \pm 1$) we obtain

$$\Phi_p^{(m_\ell)}(\mathbf{r}) = \frac{A}{r} e^{-\kappa r} \left[1 + \frac{1}{\kappa r} \right] Y_1^{m_\ell}(\theta_r, \varphi_r). \quad (29)$$

Of course, κ and the prefactor A in Eqs. (28) and (29) depend upon the particular anion and its ionization potential.

2. Fourier transform of the wave function

The Fourier transform of the bound state $\Phi_0(\mathbf{r})$ is given by Eq. (23). By making use of the plane-wave decomposition into spherical harmonics [36],

$$e^{i\mathbf{p}\cdot\mathbf{r}} = 4\pi \sum_{\ell'=0}^{\infty} \sum_{m_\ell'=-\ell'}^{\ell'} i^{\ell'} j_{\ell'}(\kappa r) Y_{\ell'}^{m_\ell'*}(\theta_p, \varphi_p) Y_{\ell'}^{m_\ell'}(\theta_r, \varphi_r), \quad (30)$$

where $j_\ell(\kappa r)$ are the spherical Bessel functions of the first kind, $\tilde{\Phi}_0(\mathbf{p})$ takes the form

$$\begin{aligned} \tilde{\Phi}_0(\mathbf{p}) &= 4A \sqrt{2\kappa\pi} (-i)^\ell Y_\ell^{m_\ell}(\theta_p, \varphi_p) \\ &\times \int_0^\infty dr r^{3/2} K_{\ell+1/2}(\kappa r) j_\ell^*(\kappa r). \end{aligned} \quad (31)$$

In particular, for the s orbitals we obtain

$$\tilde{\Phi}_s(\mathbf{p}) = \frac{2\sqrt{\pi}A}{\kappa^2 + \mathbf{p}^2}, \quad (32)$$

and from the definition of $\tilde{\Phi}_0(\mathbf{p})$ in Eq. (22),

$$\tilde{\Phi}_s(\mathbf{p}) = -\frac{4\sqrt{\pi}Ai}{(\kappa^2 + \mathbf{p}^2)^2}. \quad (33)$$

Proceeding in the same way, we find out that the Fourier transform for p states is

$$\tilde{\Phi}_p^{(m_\ell)}(\mathbf{p}) = -4i\pi A Y_1^{m_\ell}(\theta_p, \varphi_p) \frac{p}{\kappa(\kappa^2 + \mathbf{p}^2)}, \quad (34)$$

where p , θ_p , and φ_p are the magnitude, polar, and azimuthal angles defining the vector \mathbf{p} . (According to our convention, the $p_x p_y$ plane corresponds to $\theta_p = \pi/2$ and the $p_x p_z$ plane corresponds to $\varphi_p = 0$ and π .) Moreover, from Eqs. (22) and (34), the functions $\tilde{\Phi}_p^{(m_\ell)}(\mathbf{p})$ for each magnetic quantum number m_ℓ are

$$\tilde{\Phi}_p^{(-1)}(\mathbf{p}) = \frac{\sqrt{6\pi}A}{\kappa(\kappa^2 + \mathbf{p}^2)} \left(\mathbf{e}_x - i\mathbf{e}_y - \frac{2(p_x - ip_y)}{\kappa^2 + \mathbf{p}^2} \mathbf{p} \right), \quad (35)$$

$$\tilde{\Phi}_p^{(0)}(\mathbf{p}) = \frac{2\sqrt{3\pi}A}{\kappa(\kappa^2 + \mathbf{p}^2)} \left(\mathbf{e}_z - \frac{2p_z}{\kappa^2 + \mathbf{p}^2} \mathbf{p} \right), \quad (36)$$

$$\tilde{\Phi}_p^{(1)}(\mathbf{p}) = -\frac{\sqrt{6\pi}A}{\kappa(\kappa^2 + \mathbf{p}^2)} \left(\mathbf{e}_x + i\mathbf{e}_y - \frac{2(p_x + ip_y)}{\kappa^2 + \mathbf{p}^2} \mathbf{p} \right). \quad (37)$$

Here, \mathbf{e}_x , \mathbf{e}_y , and \mathbf{e}_z are the unit vectors pointing along the x , y , and z directions, respectively. As the ground-state wave functions and their Fourier transforms have been calculated, it only remains to define the laser pulse. This will be done in Sec. IV, after we introduce the triply differential probability distribution and the topological charges in momentum space.

C. Triply differential probability distribution and total probability

We define now the differential probability distribution in momentum space $\tilde{\mathcal{P}}(\mathbf{p})$. According to the conventions used in this paper, it reads

$$\tilde{\mathcal{P}}(\mathbf{p}) = \frac{1}{(2\pi)^3} |\mathcal{A}(\mathbf{p})|^2, \quad (38)$$

such that the total probability of detachment P is

$$P = \int d^3p \tilde{\mathcal{P}}(\mathbf{p}). \quad (39)$$

This integral is performed by Monte Carlo methods (Sec. VD). In our analysis we also present the energy-angular triply differential probability distribution $\mathcal{P}(\mathbf{p})$

$$\mathcal{P}(\mathbf{p}) = \frac{d^3P}{dE(\mathbf{p})d^2\Omega_p} = \frac{m_e}{(2\pi)^3} |\mathbf{p}| \cdot |\mathcal{A}(\mathbf{p})|^2, \quad (40)$$

where $E(\mathbf{p}) = \mathbf{p}^2/2m_e$ is the asymptotic kinetic energy of the electron and Ω_p is the solid angle of detection.

D. Topological charges in momentum space

In Sec. II we have shown how to calculate the topological charges in position representation. Moreover, it is possible to calculate them in any parametric space of arbitrary dimensions. This is related to the so-called Berry connection [37]. In particular, we are interested in calculating the topological charges in momentum representation. Given the probability

amplitude of detachment $\mathcal{A}(\mathbf{p})$, it can be shown that the topological charges $m(p_r, p_z)$ at $t \gg T_p$ are given by (see, e.g., Refs. [20,28] and references therein)

$$m(p_r, p_z) = \frac{1}{2\pi} \int_0^{2\pi} d\varphi_p \frac{\text{Im}(\mathcal{A}^*(\mathbf{p})\partial_{\varphi_p}\mathcal{A}(\mathbf{p}))}{|\mathcal{A}(\mathbf{p})|^2}. \quad (41)$$

This is equivalent to Eq. (12) but in momentum space. Here, $\mathbf{p} \equiv \mathbf{p}(p_r, \varphi_p, p_z)$ is written in cylindrical coordinates such that $p_x = p_r \cos \varphi_p$, $p_y = p_r \sin \varphi_p$, and p_z is fixed. Namely, the contour \mathcal{C} in Eq. (11) is a circle of radius p_r located at a distance p_z over the $p_x p_y$ plane. Before proceeding further, we shall define our laser field.

IV. LASER PULSE

We consider the photodetachment process driven by a circularly polarized single laser pulse comprising $N_{\text{osc}} = 3$ field oscillations within a \sin^2 envelope. It is assumed that the total pulse duration is T_p ; hence, the fundamental frequency of oscillations is $\omega = 2\pi/T_p$. If ω_L is the laser carrier frequency, then $\omega_L = \omega N_{\text{osc}}$ and the corresponding wavelength is $\lambda_L = 2\pi c/\omega_L$. Note that the phase of the laser field, $\phi = \omega t$, changes from zero to 2π while t changes from zero to T_p .

The laser pulse described above (and propagating along the z axis) is defined by the oscillating electric field $\mathcal{E}(\phi)$ as

$$\mathcal{E}(\phi) = \mathcal{E}_0[F_1(\phi)\mathbf{e}_x + F_2(\phi)\mathbf{e}_y], \quad (42)$$

where

$$\mathcal{E}_0 = \mathcal{E}_{\text{at}}\sqrt{I/I_{\text{at}}} \quad (43)$$

is the peak amplitude of field oscillations and I is the maximum intensity achieved by the pulse provided that

$$\max_{\phi \in [0, 2\pi]} (F_1^2(\phi) + F_2^2(\phi)) = 1. \quad (44)$$

The shape functions $F_1(\phi)$ and $F_2(\phi)$ are

$$F_1(\phi) = \mathcal{N} \sin^2\left(\frac{\phi}{2}\right) \sin(N_{\text{osc}}\phi) \cos \delta, \quad (45)$$

$$F_2(\phi) = -\mathcal{N} \sin^2\left(\frac{\phi}{2}\right) \cos(N_{\text{osc}}\phi) \sin \delta \quad (46)$$

for $\phi \in [0, 2\pi[$ and are zero otherwise. The parameter δ determines the polarization of the pulse. In particular, for circularly polarized fields, we set $\delta = \pi/4$. In such case the normalization constant is $\mathcal{N} = \sqrt{2}$ which guarantees that Eq. (44) is satisfied. For our numerical illustrations we consider a laser field of wavelength $\lambda_L = 4000$ nm (equivalent to $\omega_L \approx 0.310$ eV), pulse duration $T_p \approx 40$ fs for $N_{\text{osc}} = 3$, and a maximum intensity $I = 2.5 \times 10^{11}$ W/cm². This type of pulse has also been considered in Ref. [20].

The vector potential associated to our light field, $\mathbf{A}(\phi)$, is obtained by integrating the electric field [Eq. (42)], i.e.,

$$\mathbf{A}(\phi) = -\frac{1}{\omega} \int_0^\phi \mathcal{E}(\phi') d\phi'. \quad (47)$$

For our choice of electric-field shape functions, the vector potential also vanishes outside the interval $\phi \in [0, 2\pi]$. Moreover, we introduce here the phase-dependent ponderomotive

energy of the electron in the laser field, $U_p(\phi)$:

$$U_p(\phi) = \frac{e^2 \mathbf{A}^2(\phi)}{2m_e}. \quad (48)$$

Its relevance will be clear in the following sections.

Our investigation concerns photodetachment driven by an ultrashort laser pulse. Such a pulse can be decomposed in its Fourier constituents, and generally contains contributions from many frequencies. Under those circumstances, the traditional concept of multiphoton ionization (where the energy spectra of photoelectrons consist of individual δ -like peaks separated by a single-photon energy) is not necessarily applicable; numerous photons of different frequency may contribute to photodetachment. Hence, it is not expected that the high-probability regions in the energy distributions of photoelectrons appear at exact integer multiples of ω_L . Nevertheless, for longer pulses the frequency bandwidth narrows around the laser carrier frequency, and sharp peaks separated by single-photon energies should be observed. This is in accordance with Ref. [22].

In Fig. 1 we show the temporal evolution of the tips of the vector potential $e\mathbf{A}(\phi)$ (left panel) and electric field $e\mathcal{E}(\phi)$ (second panel) for the laser pulse configuration considered here. Those parametric plots are created by changing the phase of the laser field from $\phi = 0$ to 2π . The curves start and end at the origin of coordinates and evolve counterclockwise. The angles (in degrees) correspond to $\varphi_A(\phi) = \arg[eA_x(\phi) + ieA_y(\phi)]$ for the vector potential and $\varphi_E(\phi) = \arg[e\mathcal{E}_x(\phi) + ei\mathcal{E}_y(\phi)]$ for the electric field. In the third frame we show the two-dimensional (nonrelativistic) extension of the so-called spiral of ionization $U_p(\varphi_A)$ [31,38–41]. It is constructed by plotting the time (phase)-dependent ponderomotive energy $U_p(\phi)$ as a parametric plot. The angle with respect to the x axis is, by definition, $\varphi_A(\phi)$ and the magnitude corresponds to $|U_p(\phi)|$. The predicting power of the spiral can be summarized in two basic points: (i) $U_p(\varphi_A)$ defines the regions in momentum space where the probability of ionization (or detachment) is maximal and (ii) interference effects are observed when the arcs of $U_p(\varphi_A)$ intersect each other. If a section of the arc is far enough from the remaining parts of the parametric curve, an electron supercontinuum is formed (ionization without interference) [42,43]. As it will be clear in the next section, the spiral describes the main features of the probability distribution of photodetachment, from a qualitative perspective, for the laser field parameters considered here.

In order to better characterize the laser pulse, it is necessary to determine its frequency components. In doing so, we first define the time-to-frequency Fourier transform of an arbitrary vector function $\mathbf{g}(t)$ as [cf. Eq. (23)]

$$\tilde{\mathbf{g}}(\omega) = \int dt e^{i\omega t} \mathbf{g}(t). \quad (49)$$

In particular we are interested in the frequency distribution of the laser pulse, which is defined as

$$|\tilde{\mathcal{E}}(\omega)|^2 = |\tilde{\mathcal{E}}_x(\omega)|^2 + |\tilde{\mathcal{E}}_y(\omega)|^2. \quad (50)$$

This is shown in the right panel of Fig. 1 for our light field (positive ω). The frequency at which the maximum appears is very close to the laser carrier frequency $\omega_L \approx 0.310$ eV, as illustrated by the red vertical line, and the full width at

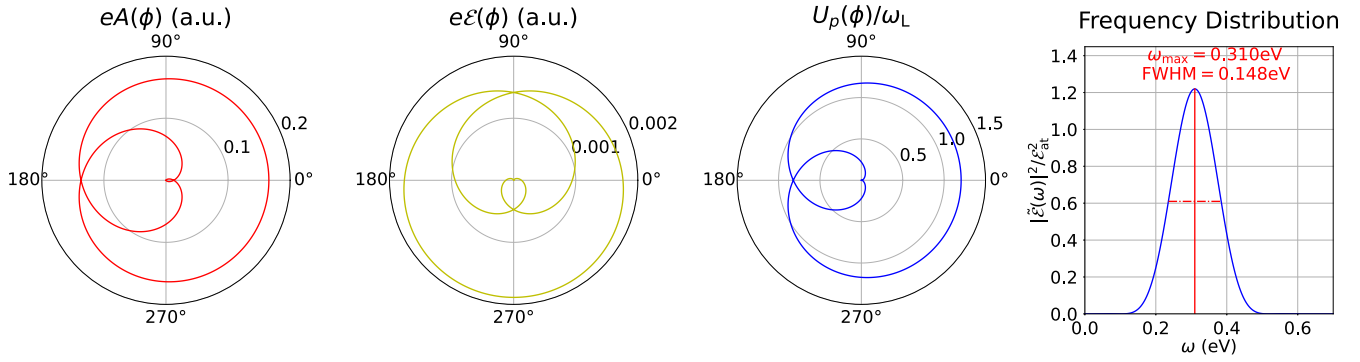


FIG. 1. Temporal evolution of the tips of the vector potential $eA(\phi)$ (left panel), electric field $e\mathcal{E}(\phi)$ (second panel), and the two-dimensional spiral of ionization $U_p(\phi)$ (third panel) as parametric plots. Those curves start and end at (0,0) and evolve counterclockwise while changing ϕ from zero to 2π . The laser pulse is defined by Eqs. (42)–(47) and comprises $N_{\text{osc}} = 3$ field oscillations. The polarization is circular ($\delta = \pi/4$) and the wavelength and intensity are fixed to $\lambda_L = 4000$ nm and $I = 2.5 \times 10^{11}$ W/cm², respectively. In the right panel we present the frequency distribution of the pulse [see Eqs. (49) and (50)] indicating the position at which its maximum is achieved (red vertical line) and the FWHM (red horizontal line).

half maximum (FWHM) is approximately 0.148 eV (red horizontal line). Thus, the ratio $\text{FWHM}/\omega_L \approx 0.5$ and photons with frequencies close to 0.310 ± 0.074 eV can participate in photodetachment.

V. VORTICITY, LASER PULSE, AND THE GROUND STATE OF THE ANION

Vortex structures in the probability amplitude of photodetachment depend on both the laser pulse characteristics and the ground-state wave function. This can be understood, as a first approach, by applying simple consideration of OAM conservation. We are dealing with circularly polarized laser pulses, hence each absorbed photon transfers one unit of \hbar to the final angular momentum of the photoelectron. For ionic systems interacting with a laser pulse, at least

$$N_{\text{min}}(\mathcal{E}_0, \omega_L) \approx \lceil (I_p + U_p(\phi_0))/\omega_L \rceil \quad (51)$$

photons need to be absorbed to promote an electron to the continuum. Here, $\lceil x \rceil$ denotes the *ceiling* function of x and $U_p(\phi_0)$ is the ponderomotive energy of the electron at its time of birth. This implies that the minimum topological charge of the resulting electron wave packet is, at least, $N_{\text{min}}(\mathcal{E}_0, \omega_L)$. The absorption of additional photons leads to the observation of the so-called multiphoton peaks in above-threshold ionization (ATI) (see Ref. [44] and, e.g., Ref. [45]) and to the increment of the total OAM by one unit of \hbar [20]. On the other hand, the initial state of the bound electron also contributes to the total angular momentum; if the electron wave function is initially found in the $(\ell, m_\ell) = (1, \pm 1)$ state, the topological charges are expected to acquire an additional $\pm\hbar$. In contrast, if the electron is found in the $(\ell, m_\ell) = (0, 0)$ or $(\ell, m_\ell) = (1, 0)$ state there is no additional OAM [21]. Therefore, as a simple rule, one expects that the topological charges $m(p_r, p_z)$ are approximately (see also Ref. [22])

$$m(p_r, p_z) \approx N_{\text{ATI}}(p_r) + N_{\text{min}}(\mathcal{E}_0, \omega_L) + m_\ell, \quad p_r > p_0, \quad (52)$$

where $N_{\text{ATI}}(p_r)$ is an integer which represents the number of multiphoton peaks (rings) surrounded by a circle of radius p_r in the three-dimensional momentum space. Furthermore, p_0 determines the region where the probability distribution starts to exhibit the multiphoton behavior (see below).

As it is stated in Ref. [7] quantum vortices can appear, in the three-dimensional space, as lines which start and end at $\pm\infty$ or as closed curves; in the intersection with a two-dimensional plane they appear either as a single point where the probability amplitude vanishes, or as two separated points with opposite circulations. (A typical example of the creation of closed vortex loops can be found in the formation of the von Kármán streets of vortices by linearly polarized laser pulses, where there is no net angular momentum transfer from photons to electrons [28,46].) It is expected that Eq. (52) is valid in the limit $p_r \rightarrow \infty$, as it arises from the conservation of total angular momentum. Therefore, such an approximation takes only into account the vortex lines which start and end at $\pm\infty$ while topological charges coming from vortex loops are not accounted for [47].

In this section we analyze the influence of the symmetry of the ground-state wave function upon the phase and magnitude of the probability amplitude of detachment. Regions in momentum space where the probability distribution vanishes determine the presence of vortex lines or nonvortex nodal surfaces. (While the former are commonly visualized as points in the intersection with a two-dimensional plane, the latter appear as lines.) To distinguish among them, we calculate the amplitude's phase. If the phase changes continuously from zero to 2π around a nodal point then we have a vortex line. In contrast, if the phase jumps by π while crossing a nodal line we have a nonvortex nodal surface. In addition, we calculate the total topological charge $m(p_r, p_z)$ [Eq. (41)] as a function of p_r . This is especially useful to detect infinite vortex lines and loops for which vortices and antivortices are sufficiently well separated.

As our main objective is to understand the influence of the symmetry of the wave function in photodetachment, we first

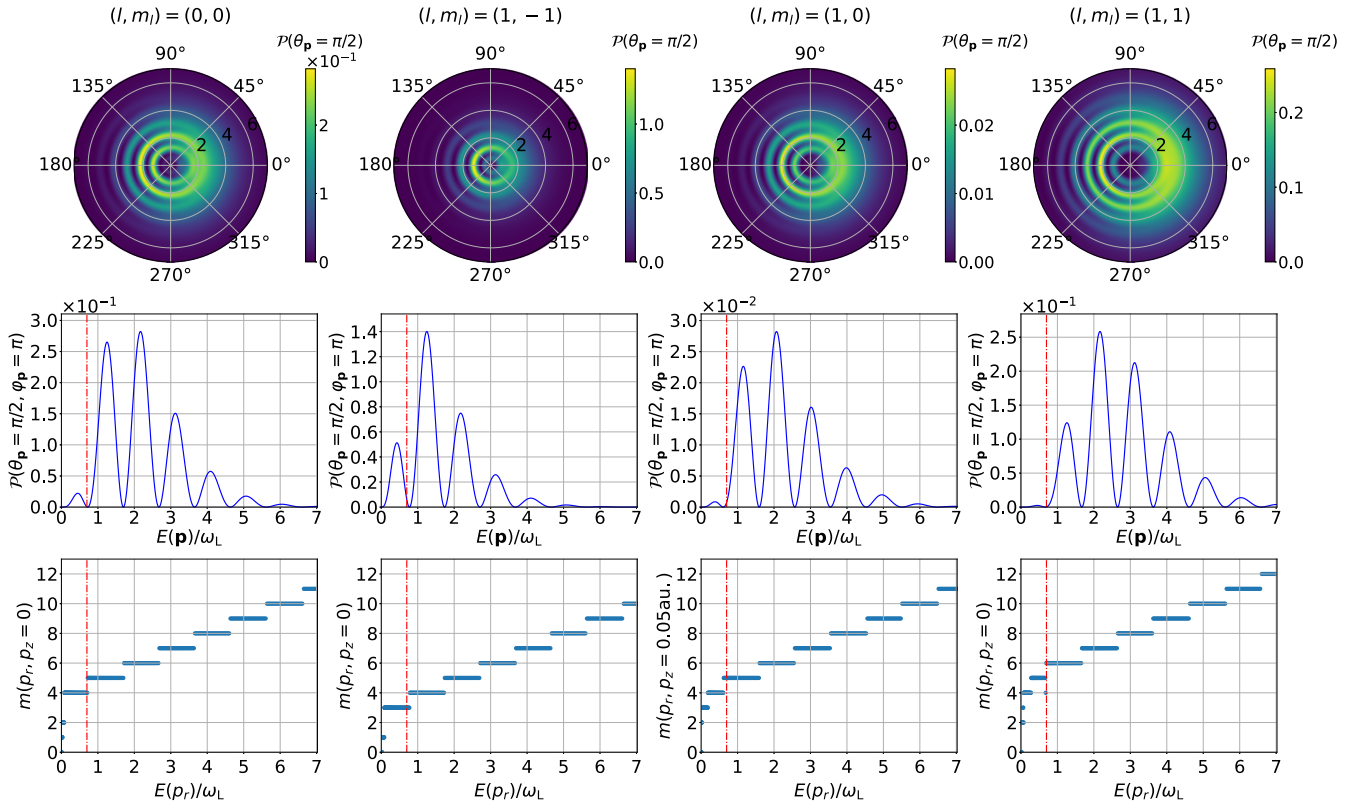


FIG. 2. In the upper panels we show the triply differential probability of detachment $\mathcal{P}(\mathbf{p})$ [Eq. (40)] in the $p_x p_y$ plane ($\theta_p = \pi/2$) as a function of the scaled kinetic energy $E(\mathbf{p})/\omega_L$ and the azimuthal angle φ_p . While the distribution for the $(1,0)$ state is calculated at $p_z = 0.05$ a.u. (we show its projection over the $p_x p_y$ plane), the remaining distributions are calculated at $p_z = 0$. In the second row we show the triply differential probability of detachment as a function of $E(\mathbf{p})/\omega_L$ at constant polar and azimuthal angles of electron detection, $\theta_p = \pi/2$ and $\varphi_p = \pi$. There, broad multiphotonlike peaks can be observed with deep minima between them. The vertical red line, at $E(\mathbf{p}) \approx 0.7\omega_L$, locates the transition from the central region to the multiphoton regime, and its position is similar for all distributions. In the third row we present the topological charges $m(p_r, p_z)$ calculated from Eq. (41) as a function of the energy $E(p_r)/\omega_L = p_r^2/(2m_e\omega_L)$. The contour \mathcal{C} is a circle of radius p_r , parallel to the $p_x p_y$ plane and at a distance p_z from the origin of coordinates. Note that, in all cases, $m(0, p_z) = 0$. The laser pulse is as defined in Fig. 1 and the target anion is H^- for the s state [20] and a model anion A^- for p states.

start by considering an H^- and A^- toy model. By this we mean that for the s states we analyze the photodetachment from the well-known H^- (see Ref. [20]) while we assume that there is another anion A^- which has the exact same ionization potential but can be found in the unperturbed p state (i.e., only the symmetry of the wave function is changed while the remaining ionic and laser field parameters remain the same). In doing so, we identify the differences in vorticity arising only from the symmetry of the bound state. After that, we shall consider photodetachment from other anions as O^- and K^- such that the influence of the ionization potential can also be determined.

A. H^- and A^- toy model

We start by considering the H^- anion and A^- model. We assume the existence of the A^- anion with the exact same ionization potential (I_p) as H^- but with a wave function in the p states. Hence, the parameters defining the ground-state wave function are, in both cases, $\kappa = 0.2354$ and $A = 0.75$ [27], for which $I_p = -E_0 = 0.754$ eV.

In the upper row of Fig. 2 we show the triply differential probability distribution of photodetachment in the $p_x p_y$

plane, $\mathcal{P}(\mathbf{p})$ with $\theta_p = \pi/2$ [Eq. (40)], as a function of the electron kinetic energy in units of the single-photon dominant frequency, $E(\mathbf{p})/\omega_L = p^2/(2m_e\omega_L)$, and the azimuthal angle φ_p . Each panel corresponds to a different initial ground-state wave function, characterized by the azimuthal and magnetic quantum numbers (ℓ, m_ℓ) , as indicated in the upper part of the figure. The left column shows the results for H^- (s orbital) and the three right columns are for the A^- model (p orbitals with $m_\ell = -1, 0, 1$). All distributions are calculated at $p_z = 0$, except for the one corresponding to the $(1,0)$ state. In this particular case, the probability amplitude of detachment has a nodal plane at $p_z = 0$ [21,27], so the distribution is calculated for $p_z = 0.05$ a.u. and we show its projection over the $p_x p_y$ plane.

Already from the upper panels in Fig. 2, important conclusions can be drawn. In the first place, all probability distributions show three well-defined regions in momentum space, independently of the symmetry of the ground-state wave function. Each one of them exhibits a different qualitative behavior and can be classified within three groups: (i) a central region, located at low photoelectron energy ($E(\mathbf{p}) \leq 0.7\omega_L$), characterized by relatively low probabilities of

detachment as compared to the remaining parts of the spectrum; (ii) a modulated supercontinuum, found around the azimuthal angle of detection $\varphi_p \approx 0$ (right part of the plots), which spans from $E(\mathbf{p}) \approx \omega_L$ up to the end of the spectrum and appears as soft fluctuations of $\mathcal{P}(\mathbf{p})$ without reaching zero (no nodes); and (iii) multiphotonlike rings, located close to $\varphi_p \approx \pi$ (left part of the plots). This last region presents strong interference effects and appears as concentric rings of high probability intercalated with zones of low probability. In particular, for $\varphi_p = \pi$, deep minima separated by roughly ω_L can be observed. Those characteristics can be traced back to the spiral of ionization $U_p(\varphi_A)$ (outer rings) shown in the third panel of Fig. 1. Strong interference effects are expected to appear at $\varphi_p = \pi$, where two of the external arcs of the ionization spiral intersect each other. On the other hand, a supercontinuum should be observed at the azimuthal angle $\varphi_p = 0$. As we have checked, by changing the number of field oscillations within the envelope, the position of supercontinuum and multiphoton regions can change. For instance, for $N_{\text{osc}} = 2$ or 4, the interference structures are observed at $\varphi_p = 0$ and the supercontinuum appears at $\varphi_p = \pi$. In such cases, the outermost arcs of the ponderomotive curve intersect each other at $\varphi_p = 0$.

From the perspective of quantum vortices generation, only the multiphotonlike structure and low-energy (central) region are of interest. This is because the modulated supercontinuum does not exhibit zeros between maxima (the probability amplitude never vanishes there) and thus vortices cannot be formed. We start by analyzing the multiphotonlike zone. In the second row of Fig. 2 we present the triply differential probability of detachment $\mathcal{P}(\mathbf{p})$ [Eq. (40)], at fixed polar and azimuthal angles $\theta_p = \pi/2$ and $\varphi_p = \pi$, as a function of the kinetic energy of photoelectrons $E(\mathbf{p})/\omega_L$. As before, we set $p_z = 0$ except for the $(\ell, m_\ell) = (1, 0)$ state, for which $p_z = 0.05$ a.u. The red vertical line, located at $E(p_0) = 0.7\omega_L$, indicates the approximate position of the first minimum and determines the transition from the central to the multiphoton regions. The energy spectra of photoelectrons, for all cases considered here, consist of broad peaks separated by energies close to (but not exactly equal to) ω_L . Both maximum and minimum values in the spectra of photoelectrons are found at rather similar kinetic energies independently of the quantum state (ℓ, m_ℓ) . Given that vortices can only appear at places where the probability distribution vanishes, it is expected that the change in topological charges will be very similar for all (ℓ, m_ℓ) along the multiphoton region. This is actually the case. The topological charges $m(p_r, p_z)$ [Eq. (41)] as a function of the electron energy $E(p_r)/\omega_L$ are shown in the lower row of Fig. 2. After the vertical red line, all topological charges show a stairlike structure with increments of one unit of \hbar at energies for which the zeros of the multiphoton structures are present (cf. with the middle row of the same figure). This indicates that, in fact, each zero corresponds to a new vortex, also in agreement with Ref. [22]. Their locations are, for practical purposes, independent of the ground state of the unperturbed anion.

Let us now concentrate on the maximum values of the topological charges calculated here, which are for an energy $E(p_r) = 7\omega_L$. For the quantum states (0,0) and (1,0), $m(p_r, p_z) = 11$ [with $p_z = 0$ for (0,0) and $p_z = 0.05$ a.u. for

(1,0)]. On the other hand, for the states (1, -1) and (1,1) the maximum topological charges reach $m(p_r, 0) = 10$ and $m(p_r, 0) = 12$, respectively. This confirms the observations made in Ref. [21], i.e., that the OAM of the ground-state wave function is transferred to the final electron state. Such effect increases (or decreases) the total topological charges by $\pm m_\ell$.

Up to now, three main conclusions can be drawn. First, the supercontinuum region lacks vorticity; second, the vortices generated in the multiphoton zone are independent of the ground-state azimuthal and magnetic quantum numbers; and third, the maximum topological charges are increased or decreased by m_ℓ . This is in full agreement with the predictions arising from Eq. (52). Let us now consider the topological charges at the end of the central (low energy) region, i.e., at $E(p_0) = 0.7\omega_L$ (intersection of the red vertical line with the blue one). While for larger energies $m(p_r, p_z)$ exhibits the smooth stairlike behavior, for lower energies the topological charges are not so predictable and depend upon m_ℓ . In particular, at the right of the red vertical line, we observe that $m(p_0, p_z) = 5$ for the states (0,0) and (1,0); $m(p_0, p_z) = 6$ for $m_\ell = 1$; and $m(p_0, p_z) = 4$ for $m_\ell = -1$. However, note that all multiphotonlike zones behave in a very similar way independently of ℓ or m_ℓ ; the main difference is a global upward or downward shifting by one unit of \hbar when $m_\ell = \pm 1$. This suggests that the transference of angular momentum from the ground-state wave function (defined by the quantum numbers ℓ and m_ℓ) manifests itself in the central region (low-energy portion of the spectrum). In contrast, the stairlike behavior (multiphoton zone) remains independent of m_ℓ . This is, at least, for the target ion and laser field parameters considered here.

In Fig. 3 we show the phase ($\arg[\mathcal{A}(\mathbf{p}_\perp)]$) and magnitude $[|\mathcal{A}(\mathbf{p}_\perp)|^v]$, where $v = 0.5$ has been chosen for visual purposes] of the probability amplitude of detachment corresponding to the probability distributions shown in the upper row of Fig. 2. This time, our plots are functions of p_x and p_y from -0.14 to 0.14 a.u., which coincide with the low-energy region of the spectrum. [In fact, the semicircular line of zero probability appearing at the left part of the plots defines the boundary between multiphoton and central regions as $E(0.13 \text{ a.u.}) \approx 0.7\omega_L$.] The laser pulse parameters are the same as in Fig. 1. The left column corresponds to the photodetachment from the H^- ion in the s state (see Refs. [20,48]) while the remaining columns relate to photodetachment from the A^- anion model. As before, the probability amplitudes are calculated for $p_z = 0$, except for the (1,0) quantum state, where we have set $p_z = 0.05$ a.u. For the photodetachment from s states (left column) we see four vortices within the central region [20]. (As mentioned before, vortices manifest themselves as nodal points for which the phase of the probability amplitude changes continuously from zero to 2π around them.) This agrees with the fact that the topological charge to the left of the red vertical line in Fig. 2 (lower left panel) is equal to 4. When considering the (1, -1) state (second column of Fig. 3) only three vortices are observed, which leads to a topological charge $m(p_r \rightarrow p_0^-, 0) = 3$. For the (1,0) case (third column), again four vortices are visible. Finally, in the fourth column of Fig. 3 we show the probability amplitude for detachment from the (1,1) state, where five vortices appear.

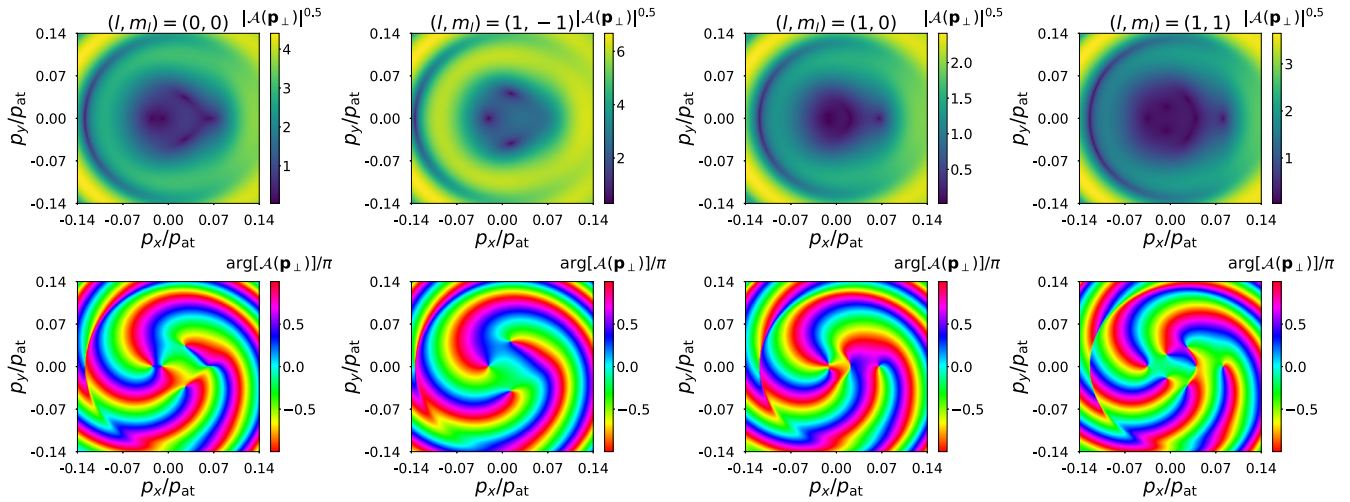


FIG. 3. Magnitude (upper row) and phase (lower row) of the probability amplitude of detachment in the two-dimensional momentum space $\mathcal{A}(\mathbf{p}_\perp)$ [Eq. (20)]. The magnitude $|\mathcal{A}(\mathbf{p}_\perp)|^\nu$ is raised to the power $\nu = 0.5$ for visual purposes and all plots are obtained by setting $p_z = 0$ (i.e., in the $p_x p_y$ plane), except for the case (1,0). There $p_z = 0.05$ a.u. The driving laser pulse is described in Fig. 1. Each column corresponds to a different ground-state wave function. While the left column shows the results for the H^- ion in the s state [20,48], the remaining columns are for the model A^- anion in the p states.

It is interesting to notice that the topological charges just before p_0 (i.e., at the low-energy region) are equal to 4 when $m_\ell = 0$. As it was mentioned above, an electron needs to absorb at least $N_{\min}(\mathcal{E}_0, \omega_L)$ photons to be promoted to the continuum [see Eq. (51)]. However, it is not known what is the value of the ponderomotive energy of the electron in the laser field at its time of birth, $U_p(\phi_0)$. Note that one of the most important features of the curve $U_p(\phi_A)$ (see Fig. 1) is its directional nature: Electrons detected with different ϕ_A angles experienced different ponderomotive energies during the detachment process [38,40]. As we are interested in the momentum region between central and multiphoton zones, it is reasonable to choose the value $U_p(\phi_0) = U_p(\phi_A = \pi)$, which is approximately $0.256 \text{ eV} = 0.83\omega_L$. Hence, from Eq. (51), the minimum number of photons required for photodetachment from H^- or A^- is actually 4. This explains why the total topological charges in the low-energy region are equal to 4 for $m_\ell = 0$.

B. O^- anion

Up to now our analysis was based on a model where the ionization potential of the A^- anion is the same as the H^- . In order to continue our investigations it is necessary to consider another anion with a different ionization potential. Our choice is O^- , which can be found in the ground-state configuration $[\text{He}]2s^2 2p^5$, i.e., it has five electrons in the $2p$ state. As before, we assume a short-range potential model for which the unperturbed ground-state wave function is described by Eq. (29) with the parameters $\kappa = 0.328$ a.u. and $A = 0.42$ a.u., for which $I_p = 1.46$ eV. Those parameters are suggested in Ref. [29]. The main difference between this system and the A^- model is that the ionization potential is almost twice for O^- (the symmetry of the wave functions is the same). Therefore, more photons need to be absorbed by the system and we expect to observe

richer vortex patterns in the low-energy region of the spectrum.

In the upper row of Fig. 4 we present the triply differential probability distribution $\mathcal{P}(\mathbf{p})$ [Eq. (40)] as a function of $E(\mathbf{p})/\omega_L$ and the angle φ_p for the photodetachment from the O^- anion. The laser field parameters are the same as described in Fig. 1. We see that the three regions observed before (supercontinuum, multiphotonlike, and central regions) are also present here. In the second row of the same figure we show the energy spectra of photoelectrons for $\varphi_p = \pi$ and $\theta_p = \pi/2$. In all cases, series of broad peaks separated by energies of around ω_L are observed. As before, the red vertical line defines the boundary between central and multiphoton regions but this time it is located at $E(p_0) = 0.47\omega_L$. At its right the topological charges (bottom row of the same figure) present a stairlike pattern with uniform increments at the points where the multiphoton zeros are found. By looking at the left of the red (vertical) line, the blue curves indicate that $m(p_r \rightarrow p_0^-, p_z) = 5$ for the quantum state (1, -1), $m(p_r \rightarrow p_0^-, p_z) = 6$ for (1,0), and also $m(p_r \rightarrow p_0^-, p_z) = 6$ for (1,1). Nevertheless, for the latter case, the topological charge jumps by two units of \hbar when the transition to the multiphoton region occurs. This implies that one of the central vortices appears very close to the border between the two regions. Thus, we corroborate our previous observation; the OAM of the ground-state wave function is transferred to the final electron state *only* in the low-energy region or at its border.

In Fig. 5 we show the same as in Fig. 3 but for the O^- ion (only p states). The range in momentum for which the probability amplitude is plotted coincides with the central region. As expected, rich patterns of vortices can be found in the distribution. In particular, for the (1,0) state (middle column), the vortices are located at the corners of a regular pentagon with an additional one at its center. It is interesting to see that, for the (1, -1) state (left column), the central vortex disappears;

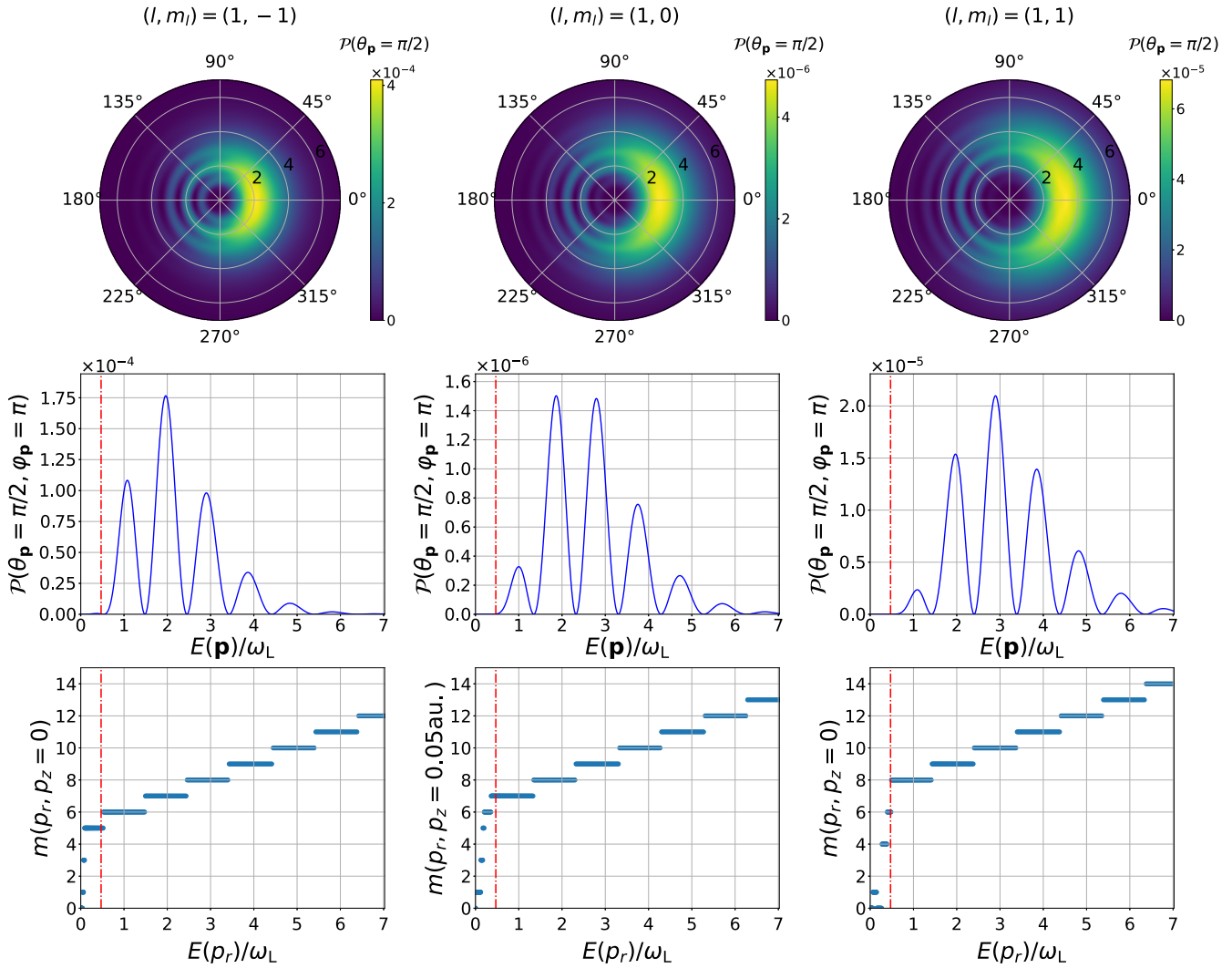


FIG. 4. The same as in Fig. 2 but for the O^- anion. This time, only the probability distributions and topological charges for p states are displayed. The ground-state wave function is defined by Eq. (29) with the parameters $\kappa = 0.328$ a.u. and $A = 0.42$ a.u. This corresponds to an ionization potential $I_p = 1.46$ eV. As before, we set $p_z = 0$ for the (1,1) and (1, -1) cases, and $p_z = 0.05$ a.u. for (1,0). In all cases, $m(0, p_z) = 0$ in the topological charge plots.

the remaining ones are relocated at the corners of another pentagon. Perhaps the most interesting case is for the state (1,1) (right column of the same figure). There, the vortices (including the one at the transition to the multiphoton region) appear at the vertices of a regular octagon. At the center of the distribution, pairs of vortices and antivortices (closed vortex loops) seem to be created along a polygon of low probability. In order to observe this better, in the upper panel of Fig. 6 we show the phase of the probability amplitude, $\arg[\mathcal{A}(\mathbf{p}_\perp)]$, as a function of the azimuthal angle $\varphi_p \in]-\pi, \pi]$ and the radius $p_r = |\mathbf{p}_\perp|$ for $0.03 \leq p_r/p_{at} \leq 0.06$, which corresponds to the central polygon. In such plot we observe the appearance of seven vortex-antivortex pairs (which correspond to closed loops in the 3D space) at different angles. Note the symmetry of the curve with respect to $\varphi_p = 0$: For each vortex located at (φ_p, p_r) , there is another one at $(-\varphi_p, p_r)$ with the same winding number, except for $\varphi_p = 0$ or π . With respect to the radial symmetry, note that the ring of low probability containing the vortex-antivortex pairs is not centered at the

origin of coordinates, and it is strongly elongated towards $\varphi_p = \pi$. For this reason, each pair of vortices appears at larger momentum for increasing $|\varphi_p|$. In the lower panel of the same figure, we show the total topological charges as a function of p_r . As expected, they jump by ± 2 units of \hbar due to this up-down symmetry, except when the first and last vortices are found (for $\varphi_p = 0$ or π), where the changes are $\pm 1\hbar$. A small misalignment between corresponding vortices leads to the single point at $m(p_r \approx 0.048 p_{at}, 0) = 0$. Finally, outside the polygon ($p_r > 0.06 p_{at}$) the total topological charge vanishes, which corroborates the presence of closed vortex loops.

From Eq. (51) it is estimated that at least $N_{min} = 6$ photons should be absorbed by the electron in order to be promoted to the continuum. This explains, in the low-energy zone, the presence of six vortices for the state (1,0), five vortices for (1, -1), and 6 + 1 vortices for (1,1), without including the one defining the boundary between central and multiphoton regions, and which is being merged into the central zone (see Fig. 5 and the discussion below). However, this simple

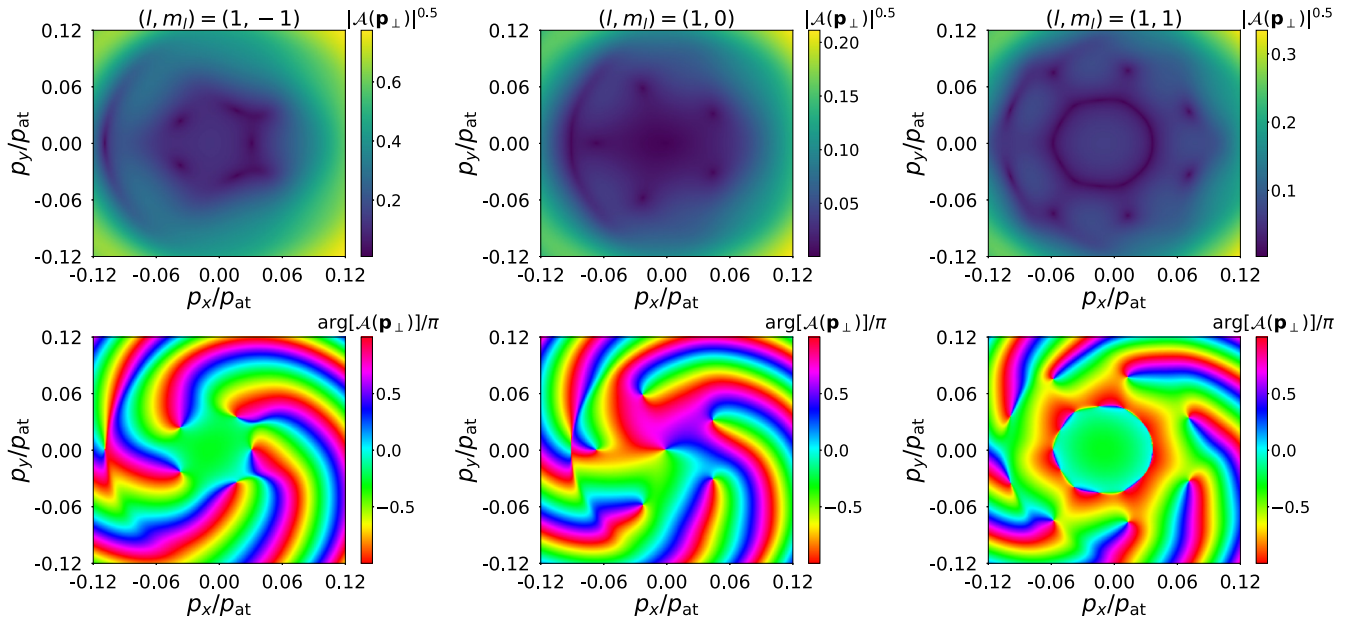


FIG. 5. The same as in Fig. 3 but for the O^- anion. Here we only present the results for p states. The parameters determining the ground-state wave function are $\kappa = 0.328$ a.u. and $A = 0.42$ a.u. such that $I_p = 1.46$ eV [see Eq. (29)]. All distributions are calculated for $p_z = 0$, except for the case (1,0) for which $p_z = 0.05$ a.u.

estimate cannot give us information about the presence of closed vortex loops at the inner polygon.

It is now interesting to analyze the changes of topological charges towards the end of the central region for the O^- anion. We have seen that, while the states characterized by $m_\ell = -1$ or 0 show a jump of one unit of \hbar at the transition to the multiphotonlike zone, the $m_\ell = 1$ case shows a jump of $2\hbar$. In order to understand this behavior, in Fig. 7 we show the same as in Fig. 6 but for the three states $m_\ell = -1$ (left panels), $m_\ell = 0$ (middle panels), and $m_\ell = 1$ (right panels). The red vertical line determines the approximate transition between central and multiphotonlike zones, and it is located at $p_0 = 0.1035p_{at}$. Note that the actual transition occurs very close to p_0 (mind the scale in the figure). Starting from the left panels ($m_\ell = -1$) we see a single vortex at $\varphi_p = 0$ and $p_r \approx 0.030p_{at}$ (upper left panel) which causes the topological charge to increase by one unit of \hbar (lower left panel). At $p_r \approx 0.038p_{at}$ two vortices at $\varphi_p \approx \pm\pi/2$ are detected, with the corresponding increment of two units to the total topological charge. For larger momentum two more aligned vortices are observed. At the transition from central to multiphoton regions, a single vortex at the angle $\varphi_p = \pi$ and p_r close to p_0 appears. A similar behavior is observed for $m_\ell = 0$ (middle panels), where pairs of aligned vortices may lead to an increment of $2\hbar$ of the topological charge, and a single vortex close to $\varphi_p = \pi$ defines the transition to the multiphoton regime. Note that for $m_\ell = 0$ and the range of momentum considered here, the winding number starts at $m(p_r = 0.02p_{at}, p_z) = 1$ which is consistent with the presence of the single vortex at $p_x = p_y = 0$ (see the middle lower panel of Fig. 5). Finally, for $m_\ell = 1$ (right panels), we see that the vortices are aligned with each other such that the first increment of the topological charge is of $4\hbar$, the next increment is of $2\hbar$, and finally, at the border with the multiphoton region, two more vortices are aligned (close to $\varphi_p = \pm\pi$), which causes another $2\hbar$ jump

during the transition. This alignment is the cause of a larger jump of the winding number for $m_\ell = 1$, as compared to $m_\ell = 0$ or -1 , near the vertical red line.

Vortex transference and vortex-antivortex formation: Intensity dependence

Up to now the most interesting case studied here has been the photodetachment from O^- . This is due to the rich vortex structures observed in the central region and the formation of vortex-antivortex pairs for the $m_\ell = 1$ case. Simple conservation of the total angular momentum allows us to predict the location of vortices in the multiphotonlike zone and the number of vortices in the central region. However, not much was said about their intensity dependence and the formation of vortex-antivortex pairs.

It is known that the creation of vortices in aero- or hydrodynamics depends upon the intrinsic properties of the fluid, its velocity distribution, and the forces acting over it. The formation of vortices in photodetachment depends upon the parameters defining the laser field, the symmetry of the ground-state wave function, and the ionization potential. While circularly polarized pulses stimulate the creation of single vortices [20], linearly polarized fields lead to the von Kármán streets of vortices-antivortices [28]. As we have shown here, both single vortices and vortex-antivortex pairs can be observed in the photodetachment from O^- . By applying additional simplification, e.g., by using the saddle-point method, it is possible to calculate analytically the approximate positions at which vortices appear in the multiphotonlike zone [22]. However, to identify their location in the central zone and to predict the formation of vortex loops is a difficult task; such structures appear when very subtle interference effects take place and additional analytical simplifications may lead to their misplacement. Nevertheless, some insight can be

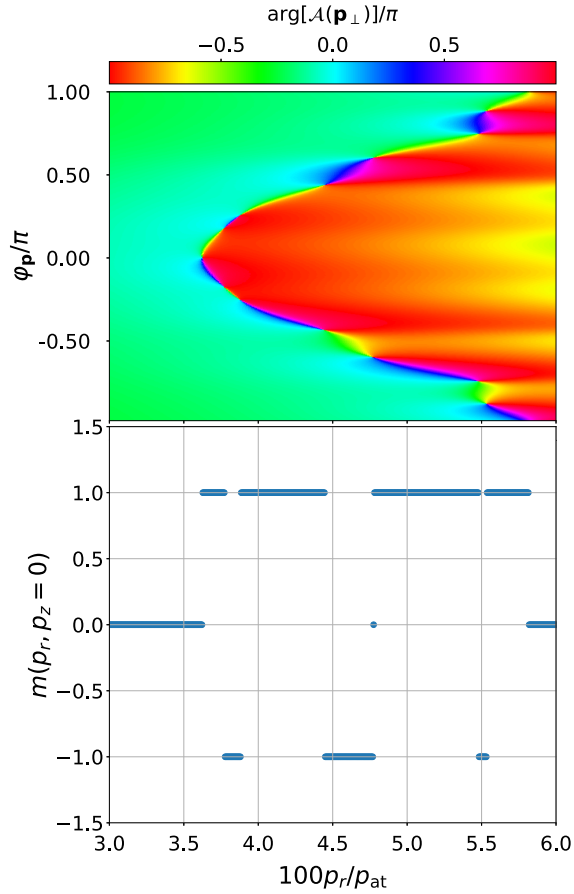


FIG. 6. Phase of the probability amplitude, $\arg[\mathcal{A}(\mathbf{p}_\perp)]$ (upper panel), and topological charges, $m(p_r, 0)$ (lower panel), for the photodetachment from O^- in the $(1,1)$ state. The laser field parameters are the same as in Fig. 1. In contrast to Figs. 4 and 5, we show here our results as a function of the azimuthal angle $\varphi_p \in [-\pi, \pi]$ and the radius $p_r = |\mathbf{p}_\perp|$, with $p_z = 0$. The range in momentum $0.03 \leq p_r/p_{\text{at}} \leq 0.06$ coincides with the central polygon of low probability shown in the lower-right panel of Fig. 5.

gained by observing in more detail the probability amplitude of detachment for the $(\ell, m_\ell) = (1, 1)$ ground state of the O^- anion.

In Fig. 8 we show the modulus of the probability amplitude of detachment $|\mathcal{A}(\mathbf{p}_\perp)|^\nu$, with $\nu = 0.5$, in the $p_x p_y$ plane ($p_z = 0$) for the O^- anion in the $(\ell, m_\ell) = (1, 1)$ state. While the laser pulse wavelength remains the same (we keep $\lambda_L = 4000$ nm), each panel corresponds to a different field intensity. Here $I_1 = 5.0 \times 10^{10}$ W/cm², $I_2 = 2I_1 = 1.0 \times 10^{11}$ W/cm², $I_3 = 3I_1 = 1.5 \times 10^{11}$ W/cm², ..., $I_{12} = 12I_1 = 6.0 \times 10^{11}$ W/cm². In the panel corresponding to I_2 we see a central region with seven well-defined vortices, identified as points of zero probability for which the phase changes from zero to 2π around them (see the corresponding panel in Fig. 9). The boundary between inner and multiphoton zones can be identified as a semicircular ring of low probability at the left part of the plot. With increasing intensity, this boundary approaches the already existing central vortices, and at $I_5 = 2.5 \times 10^{11}$ W/cm² it starts to merge into the low-energy vortical pattern. This explains the jump of two units of \hbar

close to the red line in the right panels of Fig. 7 as the first multiphoton vortex aligns itself with another one belonging to the inner zone. At higher intensities this new vortex is fully incorporated into the central region. From I_6 up to I_8 another semicircular ring (boundary) migrates towards the inner zone and after I_9 a new central vortex is observed. Such a process repeats again, generating a net vortex transfer from multiphoton to central regions. As we have checked, the same intensity dependence is observed for the $(\ell, m_\ell) = (1, -1)$ and $(1, 0)$ states of O^- (not shown). In particular, one of the boundary regions starts to merge with the central zone at $I_6 = 3.0 \times 10^{11}$ W/cm² for those two states (this is in contrast to the $m_\ell = 1$ case, where the merging happens at $I_5 = 2.5 \times 10^{11}$ W/cm²). Hence, at this higher intensity one would also observe a jump of $2\hbar$ during the transition from central to multiphoton zones.

In order to corroborate our previous observation it becomes important to analyze the phase of the probability amplitude of detachment, $\arg[\mathcal{A}(\mathbf{p}_\perp)]$, and not only its magnitude. This is presented in Fig. 9 for the same laser pulse and ion parameters as in Fig. 8. From I_2 to I_4 , it is seen that the phase changes from zero to 2π around the seven single points of zero probability in the central region. With increasing intensity, the disturbance characterizing the boundary zone (together with the lowest-energy multiphoton vortex) migrates towards the center of the plot. At the intensity $I_5 = 2.5 \times 10^{11}$ W/cm² the traveling vortex enters the central region and the formation of a new disturbance at larger momentum (left part of the plot) is observed. This vortex migration and transference continues for the intensity range considered here. Additionally, in this figure we can observe the appearance of vortex-antivortex pairs distributed along closed rings at the center of some of the plots, i.e., for $I_1, I_2, I_5, I_8,$ and I_{11} . This happens when the boundary separating the multiphoton zone approaches closely the inner structures (see Fig. 8).

In closing this section we note that vortex transfer from the multiphoton to the central region is a direct consequence of the ponderomotive shift $U_p(\phi_0)/\omega_L$ in Eq. (51), which increases linearly with intensity. Namely, at larger intensities more photons are required for the electron to be detached. For instance, if a minimum of n photons is necessary for detachment at an intensity $I^{(n)}$, then the $n+1$ photon leads to the first multiphoton peak. If the intensity is raised to $I^{(n+1)} = I^{(n)} + \Delta I$, then $n+1$ photons cause the detachment and the $n+2$ photon leads to the first multiphoton peak (a new boundary is formed). By conservation of total angular momentum, the change from $I^{(n)}$ to $I^{(n+1)}$ implies the transference of the lowest-energy vortex in the multiphoton region to the central zone. From Eq. (51) and the rough estimate $U_p(\phi_0) \approx 0.83\omega_L$ for $I = 2.5 \times 10^{11}$ W/cm², it is expected that ΔI is close to 3.0×10^{11} W/cm². However, by inspecting the transitions shown in Figs. 8 and 9, a more accurate value is $\Delta I \approx 2.0 \times 10^{11}$ W/cm².

C. K^- anion

We consider now the photodetachment from the K^- anion. Its electronic configuration is $[\text{Ar}]4s^2$, i.e., it contains two electrons in the $4s$ state. As before, we use the ground-state wave function given by Eq. (28) with the parameters $\kappa = 0.192$ a.u. and $A = 1.24$ a.u. [29] such that $I_p = 0.502$ eV.

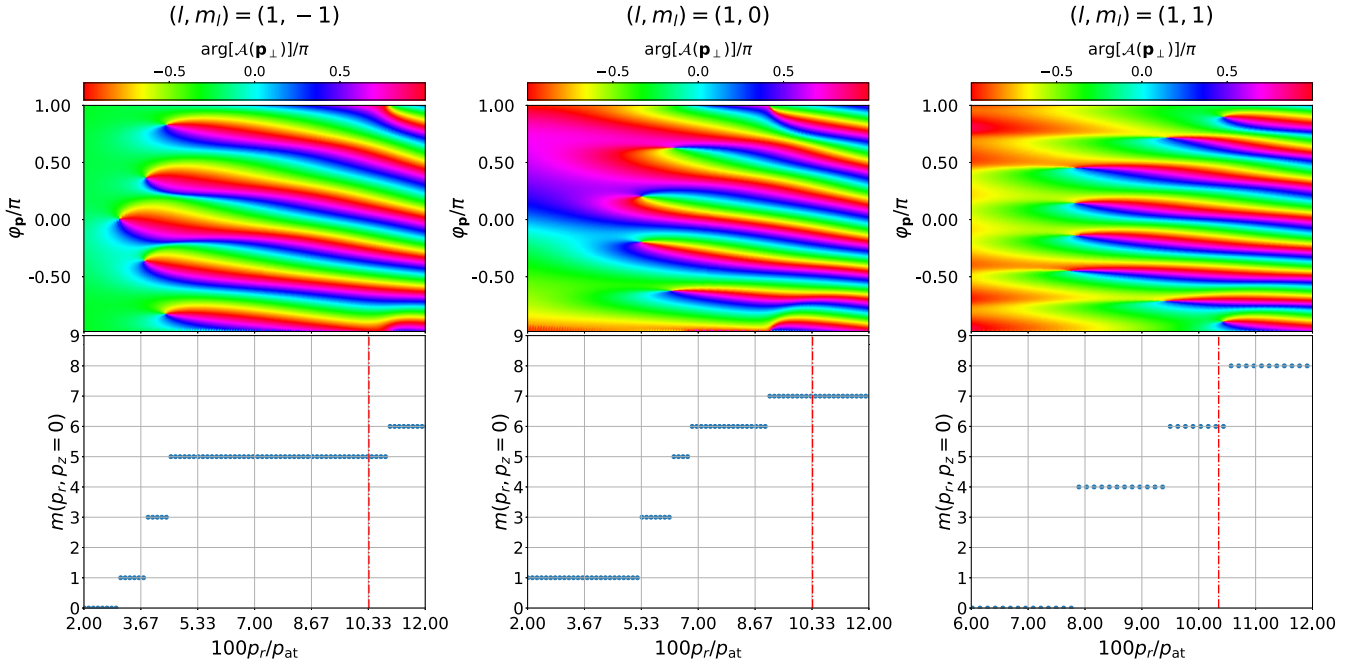


FIG. 7. The same as in Fig. 6 but for the three states $m_\ell = -1, 0, 1$. This time, the range of momentum is chosen such that the single vortices in the central region are observed. The red vertical line at $p_0 = 0.1035p_{at}$ indicates the approximate transition to the multiphotonlike zone (note that $p_0^2/2m_e = 0.47\omega_L$).

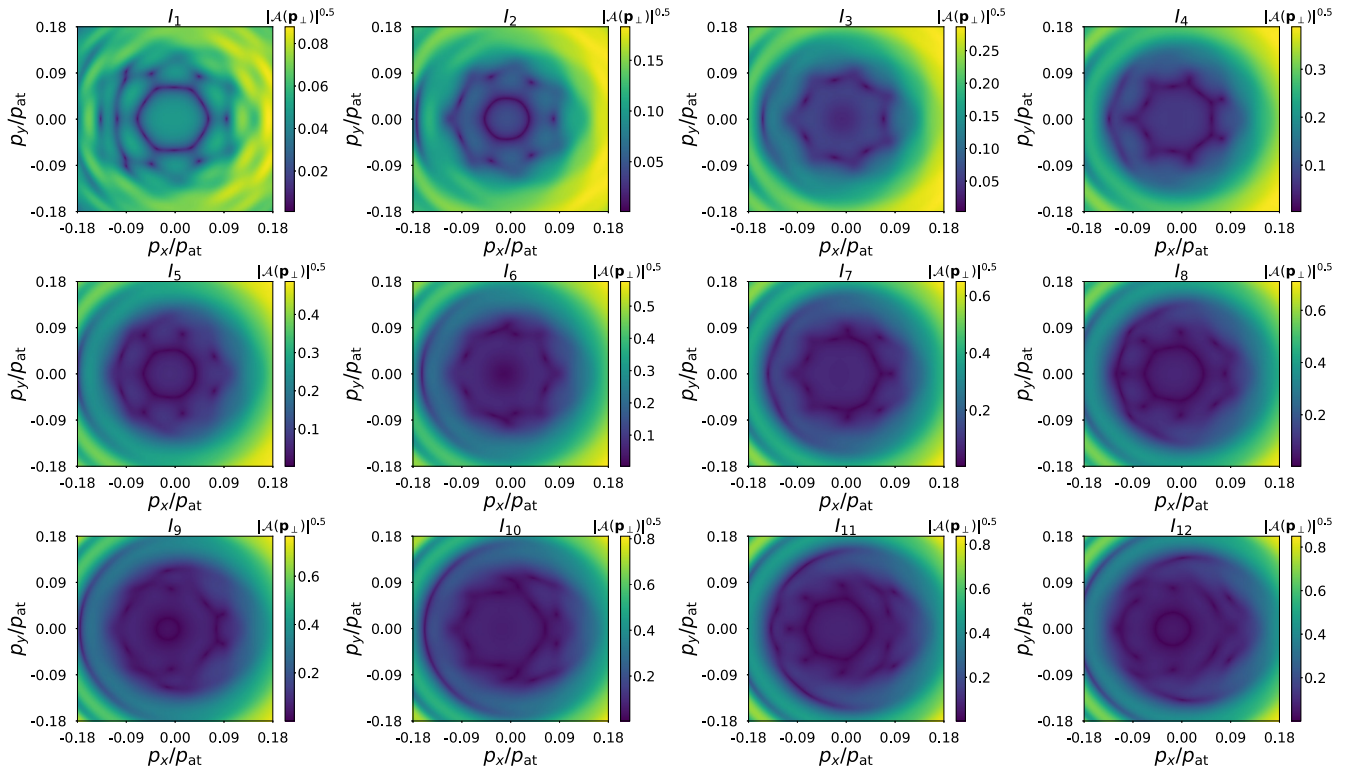


FIG. 8. Magnitude of the probability amplitude of detachment, $|A(\mathbf{p}_\perp)|^\nu$, with $\nu = 0.5$ [see Eq. (20)], in the p_x, p_y plane (i.e., $p_z = 0$). The target anion is O^- in the ground state $(\ell, m_\ell) = (1, 1)$. While each panel corresponds to a different intensity, the remaining laser field and ion parameters are the same as in Fig. 5. Here, each intensity corresponds to $I_1 = 5.0 \times 10^{10} \text{ W/cm}^2$, $I_2 = 2I_1$, $I_3 = 3I_1, \dots, I_{12} = 12I_1 = 6.0 \times 10^{11} \text{ W/cm}^2$.

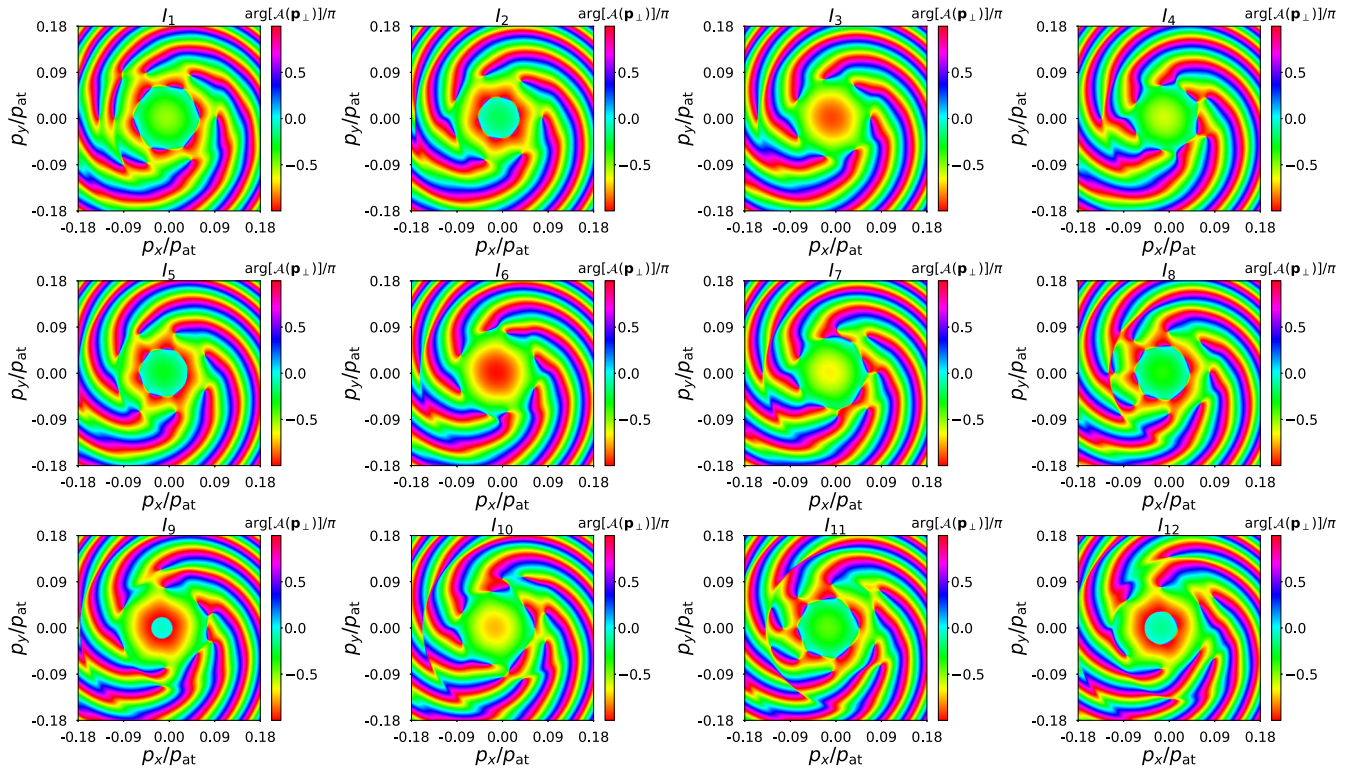


FIG. 9. The same as in Fig. 8 but for the phase of the probability amplitude of detachment, $\arg[\mathcal{A}(\mathbf{p}_\perp)]$.

This ionization potential is smaller than the one for the H^- anion (fewer photons are necessary for detachment) so we expect simpler vortex configurations in the central region of the spectrum.

In Fig. 10 we show the same as in Fig. 2 but for the K^- anion (s states and $p_z = 0$). Once again, the triply differential probability of detachment (upper panel) shows the three characteristic regions: Structured supercontinuum, central, and multiphoton zones. The topological charges (lower panel) change in a stairlike way and increase by \hbar at the energies where the zeros of the spectra of photoelectrons are found (middle panel). This is provided that we are in the multiphoton region [right of the vertical line located at $E(p_0) = 0.55\omega_L$]. To analyze the central region, in Fig. 11 we show the magnitude and phase of the probability amplitude of detachment. It can be seen that three vortices are present within the low-energy region. Note that the semicircular ring of low probability defines the boundary between central and multiphoton zones. It can be found at $p_0 \approx 0.11$ a.u., which is equivalent to $E(p_0) \approx 0.53\omega_L$.

According to the estimations in Eq. (51), the minimum number of photons required for detachment from K^- and for the laser pulse considered here is approximately $N_{\min} = 3$ photons. It also explains the fact that three vortices are observed in the probability distribution for the central region.

In closing this section we show the probability amplitude of detachment (magnitude and phase) for the detachment from K^- driven by a weaker laser pulse of intensity $I = 1.0 \times 10^{11}$ W/cm² (Fig. 12). The remaining laser field parameters are the same as in Fig. 1. By comparing Figs. 11 and 12 we see that for lower intensities both the momentum range defining the central region and the number of vortices

in it are reduced. Instead of observing three vortices now we have only two. This can be explained from Eq. (51): as the ponderomotive energy of the electron is proportional to the maximum intensity of the laser field, we obtain now $U_p(\varphi_A = \pi) \approx 0.102$ eV. Thus, the minimum number of photons for detachment at lower intensities is two photons.

D. Total probability of detachment

As it was shown in Refs. [20,28] the strong-field approximation gives impressive results for photodetachment from negative ions. The results arising from the SFA and the TDSE differ by a scaling factor often close to 1. This can be explained by the absence of a Coulomb tail in photodetachment and the low-probability of rescattering events when the process is driven by circularly polarized pulses. However, the SFA may lead to unphysical results when the total probability of detachment is above 1. Hence the validity of our model is only ensured provided that $P < 1$. In order to check that this condition is fulfilled, we estimate the total probability of detachment P [see Eqs. (38) and (39)] by Monte Carlo integration with at least 1×10^6 points, until convergence is achieved. The error is always less than 1%. We present our estimations for all cases considered here in Table I. By inspecting the right column in this table, we see that all probabilities are smaller than 1. Hence, we are within the range of validity of our model.

VI. CONCLUSIONS

We have analyzed the laser-assisted photodetachment driven by ultrashort laser pulses. By calculating the proba-

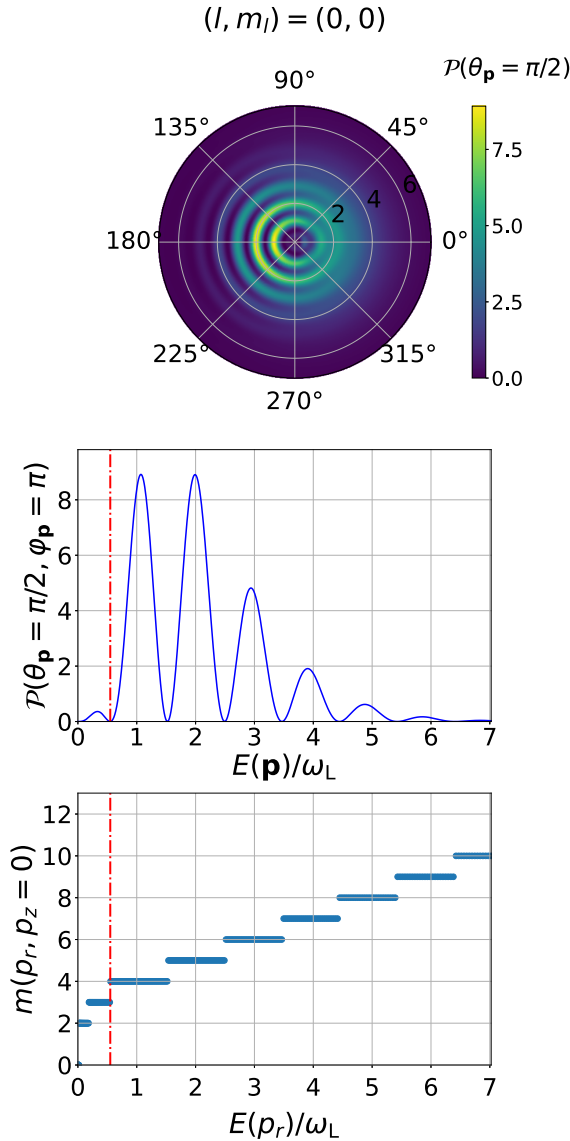


FIG. 10. The same as in Figs. 2 and 4 but for the K^- anion. We show only the results for s states [see Eq. (28)] with the parameters $\kappa = 0.192$ a.u. and $A = 1.24$ a.u. such that $I_p = 0.502$ eV. Again, we observe that $m(0, 0) = 0$, as expected.

bility amplitude of detachment under the framework of the SFA, we have determined the regions in momentum space where vortices are formed. In particular, we have shown that the two-dimensional triply differential probability distribution contains three well-defined regions: The modulated supercontinuum, low-energy (central) zone, and multiphotonlike region. The supercontinuum spans along few single-photon energies and is characterized by a probability amplitude always larger than zero, hence no vortices are formed there. In contrast, the multiphotonlike zone shows series of peaks separated by roughly ω_L and vortices can be found between them. This is a consequence of the conservation of angular momentum, as each absorbed photon carries an OAM equivalent to one unit of \hbar . Along this region, the topological charges change in a stairlike pattern with increments of \hbar when the zeros of the probability amplitude are found. This implies

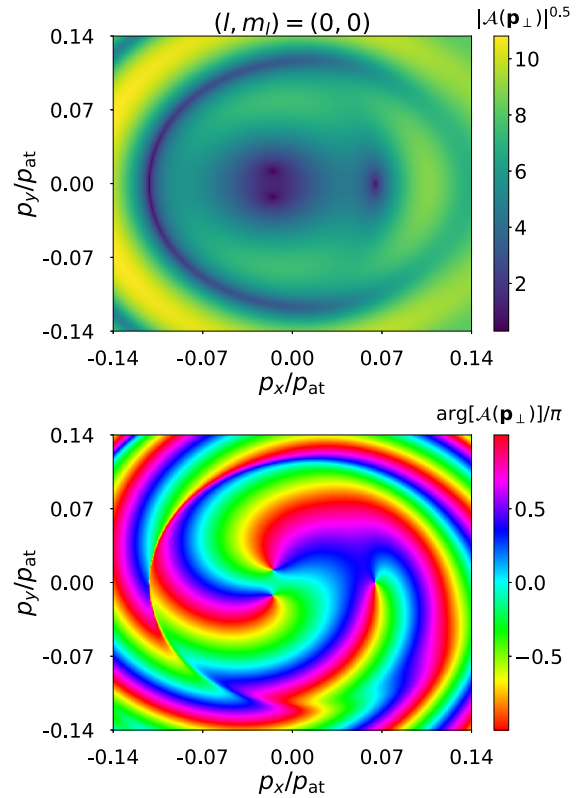


FIG. 11. The same as in Figs. 3 and 5 but for the K^- anion. Due to the electron configuration of the ion, only the results for s states are displayed. The probability amplitude of detachment is calculated for the ground-state wave function in Eq. (28) with the parameters $\kappa = 0.192$ a.u. and $A = 1.24$ a.u. ($I_p = 0.502$ eV).

that the vorticity along the multiphoton zone is determined mostly by the characteristics of the laser pulse (polarization, frequency, and duration).

The central (low-energy) region behaves differently as compared to the other ones; the number of vortices depends upon the ionization potential of the target ion and its

TABLE I. Total probability of detachment P [Eq. (39)] for the target anions considered in this paper. The driving laser pulse is as described in Fig. 1. The numerical data are obtained from Monte Carlo integration with 1×10^6 points, ensuring that convergence is achieved, and the error is not larger than 1%. We also present the electron configuration and the ionization potential (I_p) of the anion. The (ℓ, m_ℓ) state for each unperturbed ground-state wave function is also specified.

Anion	I_p (eV)	Configuration	(ℓ, m_ℓ)	P
H^-	0.754	$2s^2$	(0,0)	0.0278
A^-	0.754		(1, -1)	0.1205
			(1,0)	0.0058
O^-	1.46	[He] $2s^2 2p^5$	(1,1)	0.0276
			(1, -1)	3.151×10^{-5}
			(1,0)	6.672×10^{-7}
K^-	0.502	[Ar] $4s^2$	(0,0)	4.930×10^{-6}

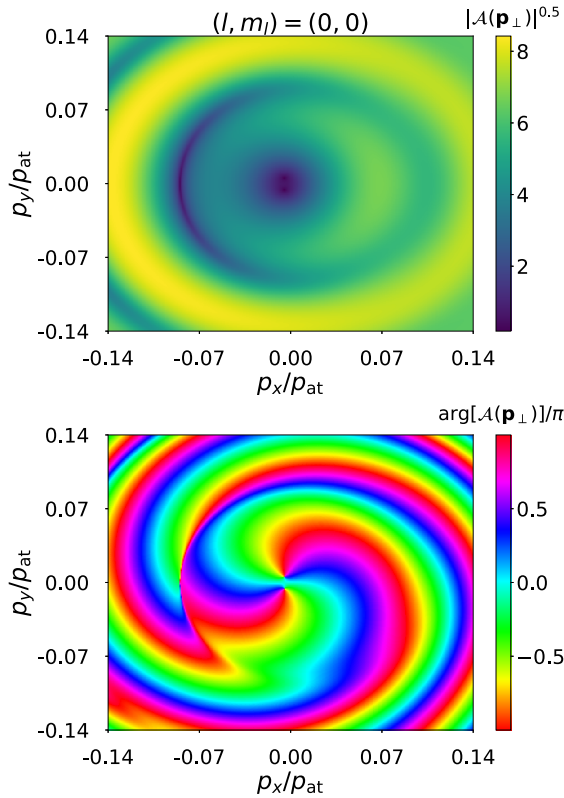


FIG. 12. The same as in Fig. 11 but for a weaker driving field. While the intensity is now $I = 1.0 \times 10^{11}$ W/cm², the remaining field parameters are the same as in Fig. 1.

ground-state wave function. For instance, the larger I_p , the greater number of vortices can be observed. This is also a consequence of OAM conservation, as more photons need to be absorbed in order to detach the electron. Furthermore, the OAM transference from the ground-state wave function to the final electron state seems to happen only at the low-energy

portion of the spectrum, at least for the laser field parameters considered here. Additionally, we show that pairs of vortices-antivortices (closed loops) can be formed in the central zone. According to the numerical explorations presented here, the central region is characterized by low probabilities of detachment as compared to the multiphoton rings. This could make difficult the experimental observations of vortices there [23]. However, the vortical structures in the low-energy zone determine, up to a large extent, the total topological charge of the electron wave packet and may contribute importantly to its behavior, evolution, and propagation in position representation.

In contrast to Ref. [20], we have analyzed here the role of the ground-state wave function, the ionization potential, and the ponderomotive shift over the formation of quantum vortices in photodetachment. We have shown that the electron momentum distribution strongly depends upon those parameters. First, the angular momentum transfer from the bound state to the freed electron happens at the central region or at the boundary between low-energy and multiphoton zones. This implies that at $p_r > p_0$ the total topological charges are increased or decreased by m_ℓ . Furthermore, depending on the symmetry of the wave function, single vortices and rings containing vortex-antivortex pairs can also be formed. Second, the ionization potential of the anion modifies importantly the number of vortices observed at the central zone: Larger ionization potentials lead to richer vortical structures. Third, the ponderomotive shift plays a crucial role in the vortex transfer from multiphoton zones to the inner region with increasing intensity. In particular, for the $(\ell, m_\ell) = (1, 1)$ state of the O⁻ anion, the formation of vortex-antivortex pairs occurs when a new vortex is incorporated into the central zone.

ACKNOWLEDGMENTS

This work is supported by the National Science Centre (Poland) under Grant No. 2018/31/B/ST2/01251.

I would like to give special thanks to Prof. J. Z. Kamiński for the very stimulating discussions and his insights about this and other physical phenomena.

- [1] P. A. M. Dirac, *Proc. R. Soc. A* **133**, 60 (1931).
- [2] J. O. Hirschfelder, A. C. Christoph, and W. E. Palke, *J. Chem. Phys.* **61**, 5435 (1974).
- [3] J. O. Hirschfelder, C. J. Goebel, and L. W. Bruch, *J. Chem. Phys.* **61**, 5456 (1974).
- [4] J. O. Hirschfelder and K. T. Tang, *J. Chem. Phys.* **64**, 760 (1976).
- [5] J. O. Hirschfelder, *J. Chem. Phys.* **67**, 5477 (1977).
- [6] E. Madelung, *Z. Phys.* **40**, 322 (1926).
- [7] I. Białynicki-Birula, Z. Białynicka-Birula, and C. Śliwa, *Phys. Rev. A* **61**, 032110 (2000).
- [8] I. Białynicki-Birula, T. Młoduchowski, T. Radożycki, and C. Śliwa, *Acta Phys. Pol. A* **100**, 29 (2001).
- [9] K. Y. Bliokh, Y. P. Bliokh, S. Savel'ev, and F. Nori, *Phys. Rev. Lett.* **99**, 190404 (2007).
- [10] G. Thirunavukkarasu, M. Mousley, M. Babiker, and J. Yuan, *Phil. Trans. R. Soc. A* **375**, 20150438 (2017).
- [11] S. M. Lloyd, M. Babiker, G. Thirunavukkarasu, and J. Yuan, *Rev. Mod. Phys.* **89**, 035004 (2017).
- [12] K. Y. Bliokh, I. P. Ivanov, G. Guzzinati, L. Clark, R. Van Boxem, A. Béch e, R. Juchtmans, M. A. Alonso, P. Schattschneider, F. Nori, and J. Verbeeck, *Phys. Rep.* **690**, 1 (2017).
- [13] J. M. Ngoko Djiokap, S. X. Hu, L. B. Madsen, N. L. Manakov, A. V. Meremianin, and A. F. Starace, *Phys. Rev. Lett.* **115**, 113004 (2015).
- [14] J. M. Ngoko Djiokap, A. V. Meremianin, N. L. Manakov, S. X. Hu, L. B. Madsen, and A. F. Starace, *Phys. Rev. A* **94**, 013408 (2016).
- [15] J. M. Ngoko Djiokap and A. F. Starace, *J. Opt.* **19**, 124003 (2017).
- [16] J. M. Ngoko Djiokap, A. V. Meremianin, N. L. Manakov, S. X. Hu, L. B. Madsen, and A. F. Starace, *Phys. Rev. A* **96**, 013405 (2017).

- [17] K.-J. Yuan, S. Chelkowski, and A. D. Bandrauk, *Phys. Rev. A* **93**, 053425 (2016).
- [18] K.-J. Yuan and A. D. Bandrauk, *J. Phys. B* **50**, 124004 (2017).
- [19] D. Pengel, S. Kerbstadt, D. Johannmeyer, L. Englert, T. Bayer, and M. Wollenhaupt, *Phys. Rev. Lett.* **118**, 053003 (2017).
- [20] L. Geng, F. Cajiao Vélez, J. Z. Kamiński, L.-Y. Peng, and K. Krajewska, *Phys. Rev. A* **102**, 043117 (2020).
- [21] A. S. Maxwell, G. S. J. Armstrong, M. F. Ciappina, E. Pisanty, Y. Kang, A. C. Brown, M. Lewenstein, and C. Figueira de Morisson Faria, *Faraday Discuss.* **228**, 394 (2021).
- [22] Y. Kang, E. Pisanty, M. Ciappina, M. Lewenstein, C. Figueira de Morisson Faria, and A. S. Maxwell, *Eur. Phys. J. D* **75**, 199 (2021).
- [23] L. Geng, F. Cajiao Vélez, J. Z. Kamiński, L.-Y. Peng, and K. Krajewska, *Phys. Rev. A* **104**, 033111 (2021).
- [24] L. V. Keldysh, *Zh. Eksp. Teor. Fiz.* **47**, 1945 (1964) [*Sov. Phys. JETP* **20**, 1307 (1965)].
- [25] F. H. M. Faisal, *J. Phys. B* **6**, L89 (1973).
- [26] H. R. Reiss, *Phys. Rev. A* **22**, 1786 (1980).
- [27] G. F. Gribakin and M. Yu. Kuchiev, *Phys. Rev. A* **55**, 3760 (1997).
- [28] F. Cajiao Vélez, L. Geng, J. Z. Kamiński, L.-Y. Peng, and K. Krajewska, *Phys. Rev. A* **102**, 043102 (2020).
- [29] B. M. Smirnov, *Physics of Atoms and Ions* (Springer, New York, 2003).
- [30] It is impressive that Dirac recognized the concept of nodal lines as sources of vortices more than 30 years before Nye and Berry. Those authors defined the *dislocations in wave trains* (regions in space where the amplitude of a wave function vanishes and its phase is singular) while analyzing the reflection of ultrasonic radiation [see J. F. Nye and M. V. Berry, *Proc. R. Soc. A* **336**, 165 (1974)]. Their study is considered to be the origin of the field of singular optics [12].
- [31] F. Cajiao Vélez, J. Z. Kamiński, and K. Krajewska, *Phys. Rev. A* **101**, 053430 (2020).
- [32] D. M. Wolkow, *Z. Phys.* **94**, 250 (1935).
- [33] Contrary to strong-field ionization from neutral atoms, this assumption is fully justified in photodetachment from negative ions; while in the former case the positively charged residue creates a long-range Coulomb potential (which modifies the electron dynamics in the continuum), in photodetachment the residual atom is neutral, hence the electron-core interaction decreases rapidly with distance from the parent atom.
- [34] K. Krajewska, I. I. Fabrikant, and A. F. Starace, *Phys. Rev. A* **74**, 053407 (2006).
- [35] F. W. J. Olver and L. C. Maximon, in *NIST Handbook of Mathematical Functions*, edited by F. W. J. Olver, D. W. Lozier, R. F. Boisvert, and C. W. Clark (Cambridge University, New York, 2010), pp. 262–263.
- [36] J. D. Jackson, *Classical Electrodynamics* (Wiley, New York, 1999).
- [37] M. V. Berry, *Proc. R. Soc. A* **392**, 45 (1984).
- [38] J. Z. Kamiński, F. Cajiao Vélez, and K. Krajewska, *Laser. Phys. Lett.* **14**, 075301 (2017).
- [39] K. Krajewska, F. Cajiao Vélez, and J. Z. Kamiński, *Europhys. Lett.* **119**, 13001 (2017).
- [40] F. Cajiao Vélez, J. Z. Kamiński, and K. Krajewska, *J. Phys.: Conf. Ser.* **999**, 012007 (2018).
- [41] F. Cajiao Vélez, J. Z. Kamiński, and K. Krajewska, *J. Phys. B* **51**, 055601 (2018).
- [42] K. Krajewska and J. Z. Kamiński, *Phys. Rev. A* **94**, 013402 (2016).
- [43] The supercontinuum is a region in the three-dimensional momentum space where the probability of ionization changes smoothly (no sudden peaks or valleys are present). In the energy spectra of photoelectrons it is observed as a broad lobe of high probability which expands for several single-photon energies.
- [44] P. Agostini, F. Fabre, G. Mainfray, G. Petite, and N. K. Rahman, *Phys. Rev. Lett.* **42**, 1127 (1979).
- [45] J. H. Eberly, J. Javanainen, and K. Rzażewski, *Phys. Rep.* **204**, 331 (1991).
- [46] N. V. Larionov, S. Yu. Ovchinnikov, A. A. Smirnovsky, and A. A. Schmidt, *Tech. Phys.* **63**, 1569 (2018).
- [47] For sufficiently large p_r , closed vortex lines cancel their contributions to the total OAM, thus the conservation of angular momentum cannot tell us anything about them.
- [48] The magnitude and phase of the probability amplitude of detachment from the H^- ion (s states) were already presented in Fig. 4 of Ref. [20] for a somehow smaller momentum range. The objective of showing it here is twofold: First, by comparing the left column of Fig. 3 with the left column of Fig. 4 of Ref. [20] we check that our numerical results and computational program are in full agreement with the ones in Ref. [20]. Second, it allows us to make a direct comparison between vortex structures generated from s or p states, which is, in part, the objective of this paper.